SYT11 as a Novel Gene in Congenital Myasthenic Syndromes

Jarred Lau

A thesis submitted in partial fulfillment of the requirements for the Master's degree in Science specializing in Cellular and Molecular Medicine

Department of Cellular and Molecular Medicine
Faculty of Medicine
University of Ottawa

Abstract

The congenital myasthenic syndromes (CMS) are a group of rare genetic diseases affecting the neuromuscular junction (NMJ). These syndromes affect signal transmission and result in fatigable muscle weakness. In this study we performed exome analysis of 2 CMS patient cohorts and identified *SYT11*, a synaptotagmin inhibitor of clathrin mediated endocytosis (CME), and *MGAT5B*, a glycosylation protein, as potential novel CMS genes using bioinformatic analysis on the RD-Connect Genome Phenome Analysis Platform (GPAP). To validate them, we utilized morpholino knockdown models of zebrafish orthologues *syt11a*, *syt11b*, and *mgat5b* and conducted functional assays measuring chorion activity and escape response. Our results show that co-knockdown of *syt11a/b* or *syt11b* alone (and not *mgat5b*) results in a substantial neuromuscular deficit, with ablation of chorion activity and severely reduced escape response. Immunofluorescent studies showed both motor neuron growth and NMJ formation was inhibited by *syt11a/b* knockdown. In conclusion, *syt11b* causes a severe neuromuscular phenotype in zebrafish which supports *SYT11* as a novel CMS-causing gene.

Acknowledgements

I would like to thank my supervisor, Dr. Hanns Lochmüller, for taking me on as his master's student and providing me with this amazing opportunity. Thank you to my Thesis Advisory Committee members Dr. Jodi Warman-Chardon and Dr. Tuan Bui for all your help and support. I'd also like to thank Dr. Emily O'Connor for teaching me all about working with zebrafish and for her guidance throughout this project. I would also like to thank Dr. Sally Spendiff for supporting me while the lab was getting established at CHEO. I would also like to extend my gratitude to everyone at the Ottawa Brain and Mind Institute for providing me with funding through the CNMD STaR Award. Furthermore, thank you to the patients who consented to being a part of this research through the RD-Connect system. This work would not be possible without their participation. I would like to thank all people in our ever-growing lab; Stephen Holland, Alex Manta, Dr. Anu Varghese, Brenda Barasa, Catherine Choueiri, Daniel O'Neil, Emilie Hill-Smith, Dr. Erin Beattie, Isabelle Fisette-Paulhus, James Davis, Jessica MacGregor, Kelly Ho, Dr. Kiran Polavarapu, Dr. Rachel Thompson, Laura Thompson, Malaichamy Sivasankar, Dr. Marc-Olivier Deguise, Matthew MacDonald, and Ofosu Adjei-Afriyie. I'd also like to thank Dr. Xiao Xiang, Dr. Dung Hoang, Emily Freeman, and Stephen Holland for their continued friendship and support, our coffee conversations were a vital part of this project. I would also like to extend my everlasting gratitude to my dear friend Abe Fehr, who saved me long days of tedious work by writing the code seen in section 2.4.2.1 of this thesis. Lastly, I would like to extend a heartfelt thanks to the entire community at the Children's Hospital of Eastern Ontario Research Institute. Working in such a supportive and caring community truly fosters excellence in science and I'm so happy to be a part of it.

Table of Contents

List of Tables

List of Figures

List of Abbreviations

ABCC8	ATP-Binding Cassette, subfamily C, member 8
ACh	Acetylcholine
AChE	Acetylcholineesterase
AChR	Acetylcholine Receptor
ACTA1	Actin, Alpha 1
ACVS	Animal Care and Veterinary Services
AF	Allele Frequency
AGRN	Agrin
ALG14	UDP-n-Acetylglucosaminyltransferase subunit
ALG2	Alpha-1,3/1,6-Mannosyltransferase
ANO5	Anoctamin 5
Ca2+	Calcium ions
CACNA1S	Calcium Channel, voltage-dependent, l type, Alpha-1s subunit
cDNA	Complementary Deoxyribonucleic Acid
CHAT	Choline Acetyltransferase
CHRNA1	Cholinergic Receptor, Nicotinic, Alpha polypeptide 1
CHRNB1	Cholinergic Receptor, Nicotinic, Beta polypeptide 1
CHRND	Cholinergic Receptor, Nicotinic, Delta
CHRNE	Cholinergic Receptor, Nicotinic, Epsilon polypeptide
CHRNG	Cholinergic Receptor, Nicotinic, Gamma polypeptide
CLCN1	Chloride Channel 1
CMS	Congenital Myasthenic Syndromes
CMS-EA	Congenital Myasthenic Syndrome with Episodic Apnea
CNAG	Centro Nacional de Análisis Genómico
COL13A1	Collagen, type XIII, Alpha-1
COL6A2	Collagen, type VI, Alpha-2
COL6A3	Collagen, type VI, Alpha-3
COLQ	Collagenic Tail of Endplate Acetylcholinesterase
CSMD2	Cub and Sushi Multiple Domains 2
d	Diameter
dH2O	Distilled Water
DNA	Deoxyribonucleic Acid
DOK7	Downstream of tyrosine Kinase 7
DPAGT1	Dolichyl-Phosphate n-Acetylglucosamine Phosphotransferase
DPEC	Diethylpyrocarbonate
dpf	Days Post Fertilization
DSHB	Developmental Studies Hybridoma Bank
e2i2	Exon 2 - Intron 2 border
e3i3	Exon 3 - Intron 3 border
ECM	Extracellular Matrix

FOXRED1	FAD-dependent Oxidoreductase Domain-containing protein 1
gnomAD	Genome Aggregation Database
GFPT1	Glutamine--Fructose-6-Phosphate Transaminase 1
GMPPB	GDP-Mannose Pyrophosphorylase B
GPAP	Genome Phenome Analysis Platform
GPAT2	Glycerol-3-Phosphate Acyltransferase 2
hpf	Hours Post Fertilization
HPO	Human Phenotype Ontology
HSPG2	Heparan Sulfate Proteoglycan of Basement membrane
iPSCs	Induced Pluripotent Stem Cells
KBTBD13	Kelch repeat- and BTB/poz Domain-containing protein 13
KD	Knockdown
KIF21A	Kinesin Family member 21a
LAMA5	Laminin, Alpha-5
LAMB2	Laminin, Beta-2
LMOD3	Leiomodin 3
LRP4	Low-density lipoprotein Receptor-related Protein 4
M	Molar
MACF1	Microtubule-Actin Cross-linking Factor 1
MBNL3	Muscleblind-Like splicing regulator 3
MFAP4	Microfibrillar-Associated Protein 4
MGAT5B	Alpha-1,6-mannosylglycoprotein 6-beta-n-acetylglucosaminyltransferase b
MO	Morpholino Oligonucleotide
mm	Millimeter
mM	Milimolar
MUNC13-1	UNC13 homolog A
MuSK	Muscle specific protein kinase
MYO9A	Myosin IXA
nl	Nanolitre
NMJ	Neuromuscular Junction
PBS	Phosphate Buffered Saline
PBST	Phosphate Buffered Saline with Tween
PCR	Polymerase Chain Reaction
PFA	Paraformaldehyde
PLEC	Plectin
PREPL	Prolyl Endopeptidase-Like polypeptide
PURA	Purine-Rich element-binding protein A
r	Radius
RAPSN	Receptor Related Protein of the Synapse
RT-PCR	Reverse Transcription Polymerase Chain Reaction
SB	Splice-blocking

SCN4A	Sodium voltage-gated Channel, Alpha subunit 4
SLC18A3	Solute Carrier family 18 (vesicular acetylcholine), member 3
SLC25A1	Solute Carrier family 25 (mitochondrial carrier, citrate transporter), member 1
SLC5A7	Solute Carrier family 5 (choline transporter), member 7
SNAP	Synaptosomal-Associated Protein
SNAP25	Synaptosomal-Associated Protein 25-KD
SNARE	SNAP receptor
SPR	Sepiapterin Reductase
SYB1	Synaptobrevin 1
SYT11	Synaptotagmin 11
SYT2	Synaptotagmin 2
TB	Translation-blocking
TCOF1	Treacle Ribosome Biogenesis Factor 1
TMR	Transmembrane Region
TPP1	Tripeptidyl Peptidase I
TRPV4	Transient Receptor Potential cation channel, subfamily V, member 4
TSC	Terminal Schwann Cell
TSS	Translation Start Site
TTC19	Tetratricopeptide repeat domain-containing protein 19
UNC13B	UNC13 homolog B
v	Volume
VAMP1	Vesicle-Associated Membrane Protein 1
VACHT	Vesicular Acetylcholine Transporter
VUS	Variants of Unknown Significance
WES	Whole Exome Sequencing
α-BT	Alpha Bungarotoxin

1. Introduction

Congenital Myasthenic Syndromes (CMS) are a group of rare, genetic diseases that cause signal transmission deficits at the neuromuscular junction (NMJ). Patients with this disease suffer from fatigable muscle weakness that prevents them from sustained motor activity. In severe cases, symptoms can include difficulties breathing and even death. These diseases are often difficult to diagnose as CMS has a broad phenotypic range that often leads to misdiagnosis of other myopathies or similar, but mechanistically different, diseases such as myasthenia gravis. In order to prove CMS, a genetic diagnosis is usually required. However, a large portion of putative CMS patients goes without genetic diagnosis due to gaps in understanding these diseases[1]. This study takes a translational research approach by analyzing patient exome data to provide genetic diagnoses and identify a novel CMS gene improve our understanding of the NMJ and how its dysfunction leads to the signal transmission defects seen in CMS.

1.1 Function, Development, and Maintenance of the Neuromuscular Junction

The NMJ is a key structure for producing muscle contractions by converting electrical signals from motor neurons into chemical signals which induce contraction in skeletal muscle fibres[2]. The biological pathways dictating the formation, function, and maintenance of NMJ are highly regulated as the NMJ must reliably transmit signals which produce muscle contraction under a variety of physiological conditions. The NMJ consists of three interacting cell types; the motor neuron, muscle fiber, and terminal Schwann cell (TSC), all communicating together to coordinate the differentiation and maintenance of the NMJ.

1.1.1 Signal Transmission at the NMJ

The signal transmission process (Figure 1.01) at the nerve terminal begins when an action potential is propagated down the motor neuron axon and triggers the opening of voltage-gated calcium channels (Ca_v2), causing an influx of calcium (Ca^{2+}) into the cytosol[3]. Synaptosome associated proteins (SNAPs), their receptors (SNAREs), synaptotagmins, and other vesicle trafficking proteins that are concentrated at active zones, sense increased Ca^{2+} levels and facilitate fusion of synaptic vesicles to the terminal membrane. This causes the release of acetylcholine (ACh) into the synaptic cleft[4]. Acetylcholine receptors (AChRs) concentrated around the folds of the postsynaptic structure then bind ACh and become activated, opening their ion-channel to allow influx of sodium (Na^+). This causes the region to depolarize[5]. Upon depolarization, an action potential travels outwards along the muscle cell membrane and down t-tubules to cause Ca^{2+} release from the sarcoplasmic reticulum, resulting in muscle contraction[2,6]. At the synapse, ACh must be removed from the cleft to end its action on the muscle. It is cleaved into acetate and choline by acetylcholine esterase (AChE) which is tethered by laminins to the folds of the postsynaptic membrane[7]. Choline is then taken up by the motor nerve terminal and re-synthesized in to ACh by choline acetyltransferase (CHAT) and repackaged into neurotransmitter vesicles by the vesicular acetylcholine transporter (VACHT)[8]. Filled vesicles are then shuttled back to active zones and primed for subsequent ACh release.

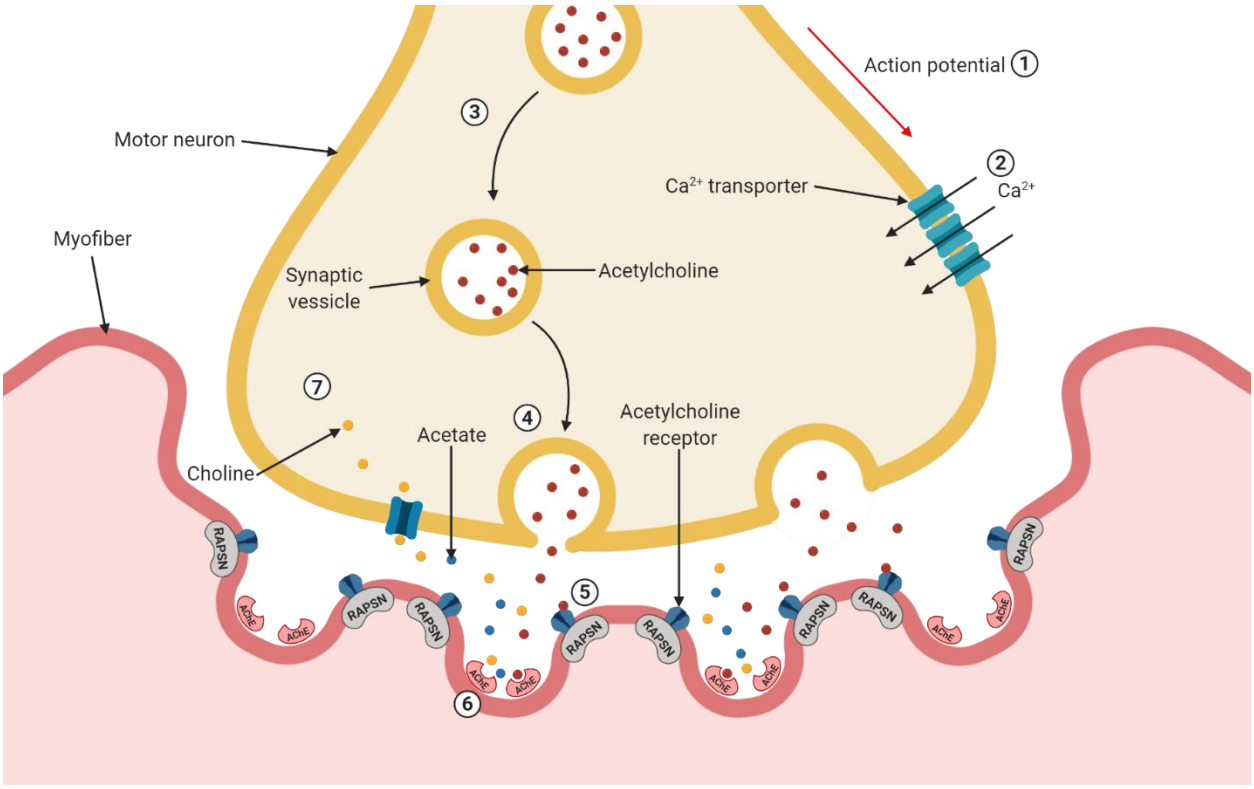

Figure 1.01 – Signal transmission at the NMJ. 1) An action potential is propagated down the motor neuron axon where it activates 2) calcium channels causing calcium influx. 3) Synaptic vesicles filled with ACh move to active zones in the terminal bulb and 4) fuse with the plasma membrane, releasing ACh into the synapse. 5) ACh binds to AChRs and cause opening of sodium channels and depolarization of the muscle fiber leading to contraction. 6) ACh in the synapse is then degraded by AChE into acetate and choline, 7) the latter of which is taken up by the motor nerve terminal for ACh synthesis and repackaging into synaptic vesicles. This figure was created with BioRender.com.

1.1.2 NMJ Development

Efficient NMJ signal transmission is dependent on the correct development and maintenance of NMJ structures. The mechanisms controlling these cellular processes involve the precise coordination of gene expression in all cell types at the NMJ. Firstly, motor neuron axons begin branching from the spinal cord and migrate towards their innervation sites utilising a host of guidance signals including semaphorins, ephrins, netrins, slits, Wnts, and other growth factors, like TGF-β1[9–12]. During migration, primitive AChR clusters begin to form before motor neuron nerve terminals arrive[13,14]. These clusters are then refined by motor neuron-secreted agrin molecules which act on the muscle via activation of the Agrin/LRP4/MuSK signalling pathway

(Figure 1.02). TSCs and approaching nerve terminals both secrete agrin, however, agrin secreted by the motor neurons (neural agrin) is much more effective at inducing AChR clustering than other sources of agrin because of specific splice inserts[15–17]. Once neural agrin binds to the MuSK/LRP4 complex, the complex is phosphorylated and Dok7 is recruited via binding of Tid1, further phosphorylating MuSK and stimulating its kinase activity[6,18]. Activated MuSK is then rapidly internalized via clathrin-dependent pathways to allow activation of Dok7 and up-regulation of actin dynamics[6]. This influences rapsyn stabilization via Hsp90β, cross-linking with actin, and direct interaction of rapsyn with AChRs allowing it to act as a scaffold for AChR clusters[18,19]. Primitive extrasynaptic AChR clusters are further refined through a negative signalling process stimulated by ACh release causing receptor dissociation[20,21].

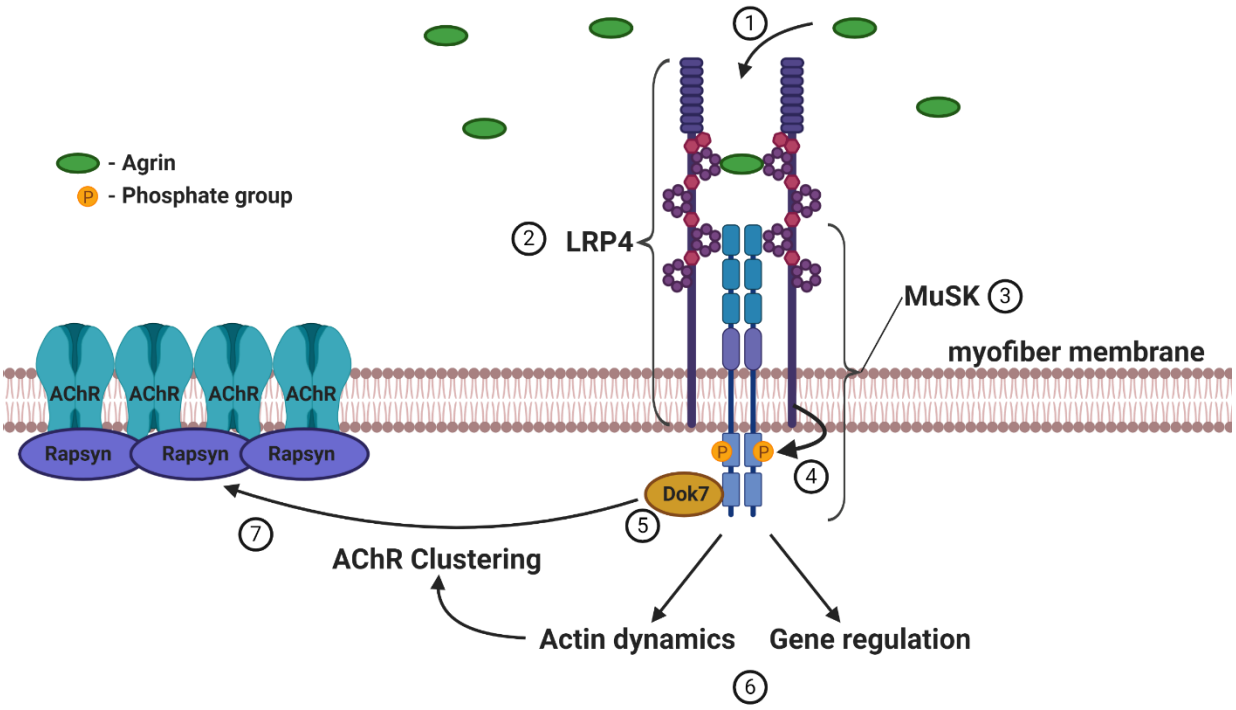

Figure 1.02 – LRP4-MuSK signalling pathway. 1) Neural agrin is secreted from approaching motor neurons and 2) binds to the LRP4-MuSK complex. 3) Binding of agrin stimulates phosphorylation of MuSK and 4) recruitment of Dok7, which 5) phosphorylates and internalizes MuSK. Internalization then activates 6) actin dynamics controlling the AChR clustering through recruitment of Rapsyn which 7) acts as a scaffolding to support AChRs, raising their density at the NMJ[10]. This figure was created with BioRender.com

On the presynaptic side, motor neurons begin the formation of active zones directly across from presynaptic folds. Presynaptic differentiation is not fully understood, but it has been shown to be induced by an agrin-independent retrograde signalling process directed by LRP4[22,23]. In this process, postsynaptic, MuSK-bound, LRP4 is cleaved by neuronal membrane-type 1 matrix metalloproteinase (MT1-MMP), travels across the synapse, and binds to a yet unknown receptor to induce active zone formation[22–24]. Upon LRP4 stimulation, these active zones are formed through organizers like laminin β2 which directly interacts with P/Q and N-type calcium channels[25,26]. These calcium channels are critical to the formation of active zones as they interact with proteins such as Bassoon, CAST/Erc2/ELKS2α, ELKS, RIMs, and Piccolo – facilitators of calcium-dependent synaptic vesicle fusion[27–32]. Once the terminal bouton has made contact with the muscle fibre, the TSCs that have migrated with the motor axon growth cone become closely associated with the NMJ to complete its formation[33]. However, multiple motor neuron nerve terminals may innervate the same site during development. Therefore, newly formed NMJs competing for the same site must undergo synapse elimination to select for the strongest terminal. TSCs help with this competition through detection and regulation of synaptic transmission strength. Upon transmission, both ATP, which is hydrolyzed into adenosine in the extracellular matrix (ECM), and ACh are released, and bind to purinergic and muscarinic receptors expressed on the TSC membrane respectively[34,35]. Activation of either of these receptors causes intracellular Ca^{2+} increase and the release of ATP, and therefore adenosine, into the ECM by the TSC[36,37]. Motor neurons then sense either low adenosine levels with A1 purinergic receptors (A1ARs) or high adenosine levels with A2 purinergic receptors (A2ARs) expressed on their surface[37]. These adenosine levels are proportional to signal transmission strength and therefore, the initial signal released by the motor neuron must be large enough to produce enough TSC-secreted

ATP/adenosine to activate A2ARs to maintain the NMJ[38]. Otherwise, the motor neuron retracts from the area leaving the NMJ with the strongest signal to innervate the fiber[38].

1.1.3 Maintenance at the NMJ

Maintenance of the NMJ seems to be involves in keeping the number of functional AChRs constant. As AChRs must be able to reliably bind ACh and cause depolarization of the muscle fiber, there are pathways by which they may be replaced or recycled[39,40]. Multiple Wnts have also been implicated in NMJ maintenance as their activity has been shown to induce AChR clustering[12]. Their action is regulated by RIG-3 which inhibits the Wnt-binding protein CAM-1[41]. This inhibition indirectly regulates the number of AChRs at the NMJ and helps prevent muscle fiber overpotentiation[41]. If injury occurs and the motor neuron is damaged the motor neuron axon will degrade and retract from the NMJ. TSCs support NMJ regeneration by extending processes which keep the motor neurons path open and acts as a guide back to the original site of innervation[42,43]. TSCs have a regulatory role during signal transduction – they help prevent acetylcholine spillover at the NMJ which would otherwise decrease signal strength[44]. These regulatory mechanisms are of critical importance to the continued function of the NMJ and demonstrate the plethora of control mechanisms the NMJ must maintain to ensure its proper function.

Efficient signal transmission at the NMJ is dependent on the correct development and maintenance of NMJ structures. The mechanisms which control these cellular processes involve the precise coordination of gene expression in all cell types at the NMJ. Mutations that occur in any of these genes may result in incorrect formation, functioning or maintenance of the NMJ, leading to inefficient signal transduction and ultimately muscle fatigability and weakness.

1.2 The Congenital Myasthenic Syndromes

1.2.1 Pathology

Common symptoms of CMS are fatigable weakness in the oculobulbar and limb muscles, general muscle weakness, and breathing difficulties in severe cases. CMS onset normally occurs in the early years of life, but in rare cases can present during teenage years[45,46]. A wide phenotypic spectrum renders diagnosing CMS difficult as there are not only many symptoms, but significant symptomatic overlap with other NMJ-related diseases. In general, patients with presynaptic CMS tend to present with a severe early onset disease, apnoea and symptoms linked to central nervous system defects[47]. Synaptic and basal-lamina associated CMS are very rare, often progressive and present with general weakness, feeding difficulty, respiratory insufficiency, ophthalmoparesis and ptosis[47,48]. Postsynaptic CMS constitute the bulk of CMS subtypes and patients and define signature CMS symptoms including decremental response upon repetitive nerve stimulation, limited eye movement, selective weakness in distal and upper limb muscles (even from birth), ptosis, muscle atrophy, and potentially fatal respiratory crises[47,49,50]. This class of CMS contains the largest number of genes, yet no clear description of a genotype-phenotype relationship. Defects in glycosylation-associated proteins are also present in CMS and these proteins exist both in the nerve terminal and postsynaptic structures, therefore patients often experience both pre- and postsynaptic symptoms[51]. The multitude of CMS symptoms partially resemble other conditions such a botulism, spinal muscular atrophy, and muscular dystrophy – thus increasing the time taken for patients to receive appropriate treatment and symptom management[48].

1.2.2 Diagnosis and Treatments

Clinical diagnoses can be made at birth based on symptom presentation such as presence of ptosis and fatigable weakness, accompanied by a decremental electromyographic response. However, these symptoms do not always manifest immediately as CMS has a particularly broad

phenotype and many genetic subtypes[51]. A decremental response may not be seen unless muscles are subject to prolonged stimulation with increasing frequency, and even then, these responses are similar to those of myasthenia gravis (an autoimmune condition)[52,53]. A positive family history is a good indicator for diagnosis if there is known consanguinity or known founder effects in a population, but the recessive nature of the disease may lead to an absence of other affected family members[53]. Therefore, diagnosis, especially in adults, may be missed until the patient develops more common symptoms. To make things more difficult, even patients with the same genetic defect can display differences in severity and type of symptoms – as is demonstrated by patients with the ε1267delG mutation in *CHRNE*[54]. To confidently diagnose and treat CMS, a genetic diagnosis or antibody tests (lack of NMJ-related antibodies) is required to distinguish CMS from myasthenia gravis[53]. However, advancements in sequencing technologies like whole exome (WES) and whole genome (WGS) sequencing have propelled CMS genetic diagnosis rates as well as discovery of novel CMS genes. 20 of the 33 known CMS genes have been discovered since 2010[55]. Yet, even with many known CMS genes, around 40% of patients are still without a genetic diagnosis[1,56]. This has implications on patient treatment as some treatment options may exacerbate symptoms in patients with certain subtypes of CMS, but provide symptomatic relief to others[51]. Pyridostigmine, an inhibitor of AChE, is a typical CMS treatment that extends the life of ACh in the synapse allowing for more AChRs to open and successfully depolarize the muscle to induce contraction. While a beneficial option for many patients, those with slow-channel syndrome experience worsening symptoms as their AChRs remain open for too long, extending the length of action potentials and making the muscle fiber less responsive to successive signals[51]. The opposite of this is seen in fast-channel syndromes where AChE inhibitors can produce positive

results. These cases highlight the importance of genetic diagnosis in patients with CMS, a critical component of a positive prognosis and improved living conditions for those with this disease.

1.2.3 CMS Genes

CMS disease genes can be grouped as presynaptic, synaptic, postsynaptic and glycosylation genes (Table 1-1)[2,47,55]. In general, the most commonly mutated CMS gene is *CHRNE* which was discovered in 2000 by Sieb *et al. CHRNE* variants now account for between 30-50% of cases world wide[55]. Mutations in *CHRNE,* encoding the epsilon subunit of the AChR, are considered a form of postsynaptic CMS[2]. Defective CHRNE leads to inefficient ACh binding and reduced capacity to produce an action potential in skeletal muscle. Mutations in *CHAT, COLQ, RAPSN, CHRNE, DOK7,* and *GFPT1* comprise about 90% of CMS cases with genetic diagnosis[55]. A recently discovered CMS gene is the ubiquitously expressed *MACF1* gene – further expanding the scope of genes linked to a CMS phenotype[57]. MACF1 is microtubule actin crosslinking factor 1 which localizes to the postsynaptic membrane of the NMJ, where it is predicted to serve as an organizing scaffold interacting through rapsyn to concentrate AChRs to the NMJ during development[57]. As discussed above, there are 33 known CMS genes with a diverse phenotypic range (Table 1-1). A variation of disease severity can be a signal that there are genetic modifiers that, in combination with mutations in known CMS genes, can cause a patient to have mild or severe disease. Researchers are working on ways to identify CMS modifiers through the use of multi-omics technologies that combine large proteomic, metabolomic, and genomic datasets in order to identify relationships otherwise undetected during human analysis[58].

	Presynaptic	Synaptic	Postsynaptic	Glycosylation
Gene	*SLC5A7* *CHAT* *SLC18A3* *SNAP25* *VAMP1* *SYB1* *SYT2* *MYO9A* *AGRN* *MUNC13-1*	*COLQ* *LAMB2* *LAMA5* *COL13A1*	*CHRNA1* *CHRNB1* *CHRND* *CHRNE* *CHRNG* *DOK7* *MUSK* *MACF1* *LRP4* *PREPL* *SCN4A* *RAPSN* *PLEC* *SLC25A1*	*GFPT1* *DPAGT1* *ALG2* *ALG14* *GMPPB*

Table 1-1: Canonical CMS genes

1.3 Zebrafish as a Model for Congenital Myasthenic Syndromes

Zebrafish have been used for decades as models of human disease. They share 70% of human genes, with 82% of known human disease genes possessing orthologues in zebrafish[59]. Zebrafish provide many advantages as a disease model. Their ability to produce hundreds of offspring provides significant statistical power to experiments. Zebrafish embryos are transparent throughout their development allowing easy observation of many internal organs and muscle structure without the need for euthanization. They also develop quickly, externally, and respire via oxygen diffusion through the skin – which bypasses potentially lethal complications of genetic knockdown in early embryonic development that may appear in other models like mice[60]. External development also allows for the fast and easy use of genetic knockdown technologies like morpholinos (oligonucleotides that sterically bind to specific RNA sequences) and clustered regularly interspaced short palindromic repeats (CRISPR)/Cas9 technologies[61].

Translational medicine has made particular use of these knockdown technologies in combination with zebrafish to quickly assess gene function. The testing of novel and known

compounds in transgenic and morphant fish have accelerated the development of novel therapies as fish can be easily treated in multi-well plates to measure dose response and toxicity. Translational neuromuscular disease (NMDs) research has taken advantage of the zebrafish model in combination with high-throughput sequencing technologies like whole exome sequencing (WES) to elucidate pathomechanisms and identify both novel genes and modifiers[60,62]. Zebrafish are of particular use in NMD research as they have well-defined timepoints of neuromuscular system development, making them useful when looking for motor defects[63].

In translational CMS research the combination of WES and morpholino knockdown in zebrafish have been successfully used to identify and validate pathogenic genes like *GFPT1, GMPPB, DOK7, MYO9A*, and *SLC25A1*[64–68]. Many common forms of CMS also have permanent zebrafish lines that are well characterized. For example, the AChR α-subunit mutations that induce slow-channel CMS produce a remarkably similar phenotype in fish which respond to human drug treatments like quinidine[69,70]. Other zebrafish lines include members of the AGRN-MUSK-LRP4 signalling pathway and range from traditional transgenic lines with specific mutations to transient morpholino knockdown models. Of note is the *twitch once*$^{(two-/-)}$ line of zebrafish which possesses a mutation in *rapsn*[71,72]. The *twitch once*$^{(two-/-)}$ line mimics a CMS phenotype showing locomotor deficits in spontaneous movement and escape response, inhibited AChR clustering, altered motor neuron axon branching and even decremental response to repetitive stimulation, showing how powerful the zebrafish model can be when investigating CMS[71,72].

1.4 Project Rationale

The number of genetically undiagnosed patients leaves room for the discovery of new CMS genes. It is important to discover new CMS genes and validate their mechanisms of action through experimentation – to allow for appropriate treatments to be prescribed or developed to account for specific genetic nuances. Our team has had success in the discovery of novel CMS genes such as *MYO9A*, where novel gene candidates were identified with exome analysis and taken in to the lab to perform knockdown studies in cells and zebrafish[67]. Similar methods of novel gene discovery were utilized in this study. Patients have already been through primary exome analysis using the Genome Phenome Analysis Platform, an online, user friendly, platform used to search for pathogenic variants in exome sequence data[73,74]. We utilized both a targeted and exome-wide search approach to identify pathogenic variants in novel genes that may have otherwise been missed during primary analysis. Novel gene candidates were then knocked down with morpholino oligonucleotides in zebrafish to determine if they cause neuromuscular transmission defects.

1.5 Aims

1. Use patient exome sequences to provide CMS patients with a genetic diagnosis in known CMS genes or to discover rare pathogenic variants in genes novel to CMS
2. Determine pathogenic mechanism of novel CMS causing genes by:
    a. Using morpholino-mediated knockdown of novel CMS genes in zebrafish
    b. Characterization of behavioral and structural differences to the neuromuscular system on novel gene knockdown in zebrafish

2. Methods

2.1 Exome Analysis of 2 CMS Patient Cohorts

2.1.1 CMS Patient Cohorts

WES was performed on whole blood samples from 2 CMS patient cohorts by multiple sequencing centres as part of European projects including deCODE Genetics, Centro Nacional de Análisis Genómico (CNAG), and the Broad Institute. All samples were collected over a period of several years by referral from expert centres across the globe and exome sequence data deposited into the RD-Connect database. Exome sequences were then analyzed for pathogenic variants by experts from Newcastle University, CNAG, and the Children's Hospital of Eastern Ontario Research Institute (CHEO-RI) using exome sequence analysis as described in section 2.2.2 or similar. Cohort 1 contained a mix of 53 clinically diagnosed male and female patients from India, Brazil, Italy, the United Kingdom, Portugal, and Romania. Of these patients there were 25 singleton cases (only patient exome data available), 5 duo pairs (patient plus father or mother), 9 trios (patient plus both parents) 2 families of 4 (patient, both parents and a sibling), and 6 sibling pairs. Cohort 2 contained 23 singleton CMS patients from Germany and Hungary, all of which had episodic apnea (CMS-EA).

Cohort	Family Number	Patient Number	Relation	Case type	Affected?
1	1	1	Index Case	sib-pair	yes
1		2	Index Case		yes
1	2	3	Mother	trio	no
1		4	Index Case		yes
1		5	Father		no
1	3	6	Index Case	sib-pair	yes
1		7	Index Case		yes
1	4	8	Index Case	trio	yes
1		9	Mother		no
1		10	Father		no
1	5	11	Index Case	singleton	yes
1	6	12	Index Case	singleton	yes
1	7	13	Index Case	singleton	yes
1	8	14	Index Case	duo	yes
1		15	Mother		no
1	9	16	Index Case	singleton	yes
1	10	17	Index Case	duo	yes
1		18	Father		no
1	11	19	Index Case	singleton	yes
1	12	20	Index Case	singleton	yes
1	13	21	Index Case	trio	yes
1		22	Mother		no
1		23	Father		no
1	14	24	Index Case	trio	yes
1		25	Mother		no
1		26	Father		no
1	15	27	Index Case	singleton	yes
1	16	28	Index Case	singleton	yes
1	17	29	Index Case	singleton	yes
1	18	30	Index Case	singleton	yes
1	19	31	Index Case	singleton	yes
1	20	32	Index Case	singleton	yes
1	21	33	Index Case	singleton	yes
1	22	34	Index Case	singleton	yes
1	23	35	Index Case	singleton	yes
1	24	36	Index Case	singleton	yes
1	25	37	Index Case	trio	yes
1		38	Father		no
1		39	Mother		no
1	26	40	Index Case	trio	yes
1		41	Mother		no

1		42	Father		no
1	27	43	Index Case	duo	yes
1		44	Mother		no
1	28	45	Index Case	trio	yes
1		46	Father		no
1		47	Mother		no
1	29	48	Index Case	sib-pair	yes
1		49	Index Case		yes
1	30	50	Father	trio	no
1		51	Mother		yes?
1		52	Index Case		yes
1	31	53	Index Case	family of 4	yes
1		54	Index Case		yes
1		55	Mother		no
1		56	Father		no
1	32	57	Index Case	singleton	yes
1	33	58	Index Case	family of 4	yes
1		59	Index Case		no
1		60	Mother		no
1		61	Father		no
1	34	62	Index Case	sib-pair	yes
1		63	Index Case		yes
1	35	64	Index Case	singleton	yes
1	36	65	Index Case	singleton	yes
1	37	66	Index Case	duo	yes
1		67	Mother		no
1	38	68	Index Case	trio	yes
1		69	Mother		no
1		70	Father		no
1	39	71	Index Case	trio	yes
1		72	Father		no
1		73	Mother		no
1	40	74	Index Case	singleton	yes
1	41	75	Index Case	singleton	yes
1	42	76	Index Case	sib-pair	yes
1		77	Index Case		yes
1	43	78	Index Case	singleton	yes
1	44	79	Index Case	sib-pair	yes
1		80	Index Case		yes
1	45	81	Index Case	duo	yes
1		82	Mother		no
1	46	83	Index Case	singleton	yes
1	47	84	Index Case	singleton	yes

1	48	85	Index Case	trio	yes
1		86	Mother		no
1		87	Father		no
2	49	88	Index Case	singleton	yes
2	50	89	Index Case	singleton	yes
2	51	90	Index Case	singleton	yes
2	52	91	Index Case	singleton	yes
2	53	92	Index Case	singleton	yes
2	54	93	Index Case	singleton	yes
2	55	94	Index Case	singleton	yes
2	56	95	Index Case	singleton	yes
2	57	96	Index Case	singleton	yes
2	58	97	Index Case	singleton	yes
2	59	98	Index Case	singleton	yes
2	60	99	Index Case	singleton	yes
2	61	100	Index Case	singleton	yes
2	62	101	Index Case	singleton	yes
2	63	102	Index Case	singleton	yes
2	64	103	Index Case	singleton	yes
2	65	104	Index Case	singleton	yes
2	66	105	Index Case	singleton	yes
2	67	106	Index Case	singleton	yes
2	68	107	Index Case	singleton	yes
2	69	108	Index Case	singleton	yes
2	70	109	Index Case	singleton	yes
2	71	110	Index Case	singleton	yes

Table 2-1: General patient information. This table describes the health status, relation, and cohort of all index cases and their family members that were included in exome analysis for this study.

2.1.2 Exome Studies with the Genome-Phenome Analysis Platform

2.1.2.1 Primary Exome Analysis

The Genome Phenome Analysis Platform (GPAP) was used to analyze patient exome sequences for pathogenic variants. We generated lists of rare variants based on standard filtering methods (Figure 2.01) including a gnomAD allele frequency of <0.001, and variants with a high or moderate probability of causing protein damage. Variants were filtered further by using parental sequences (if available) for segregation analysis. Pre-set gene lists, like the muscle gene table (www.musclegenetable.fr), and customized gene lists based on Human Phenotype Ontology terms (HPOs) from the patients clinical presentation, were also used to narrow variant lists to genes

relevant to the patients specific phenotype[75]. If known to be present in the family, consanguinity was also accounted for by looking for long homozygous runs in the patient's exome sequence. *In silico* prediction using the Human Splicing Finder was used to determine if a variant was likely to be damaging or cause alternative splicing[76]. This filtering process resulted in a manageable number of variants (~10-20) per patient for further in-depth evaluation. Evidence of gene expression in muscle or neuronal tissues from databases such as GTEx (www.gtexportal.org) was gathered. Literature searches for known roles at the NMJ were conducted, and protein-protein interaction networks were generated by using networking websites like GeneMANIA and STRING [77,78]. If a particular variant had high probability of causing damage to the protein, was expressed in muscle or neuronal tissues, or had a known role in processes at the NMJ, the variant was flagged for further investigation.

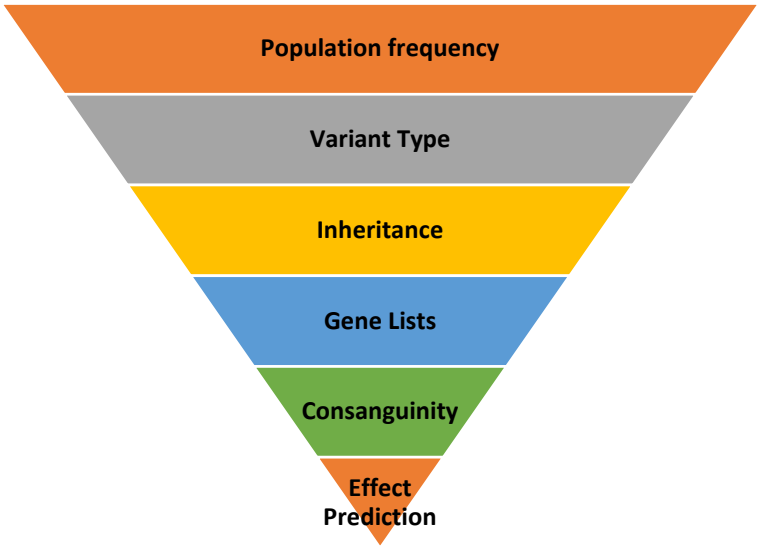

Figure 2.01 – Variant filtration with GPAP. Filtering of rare pathogenic variants begins by isolating only mutations found to be rare in the general population. Moving down a step filters variants according to their type (high, moderate, low, and modifiers). Those with incorrect inheritance can then be ruled out if found in a healthy parent. Genes are then generated with HPOs to make the search tailored to the patient. Consanguinity and finally *in silico* prediction tools then filter to a manageable candidate list.

2.1.2.2 Exome Re-analysis

If a convincing variant could not be identified by primary analysis, filters and parameters were broadened to capture cryptic variants that could be damaging. First, variants of low damage probability and modifier variants were included in exome searches. Secondly, constraints on gnomAD allele frequency were relaxed to <0.01. Thirdly, the full exome was searched – rather than a more limited number of genes from gene lists. This helped in a variety of ways, 1) It allowed for the inclusion of synonymous or intronic mutations that could generate cryptic splice sites or affect regulatory elements. 2) The relaxing of allele frequency constraints allowed for the inclusion of more common variants that in combination with rare, damaging variants could explain a phenotype (i.e., compound heterozygous variants). 3) Exome-wide searches include genes that are not yet linked to any known disease and would otherwise be excluded from targeted gene lists. The variants found from these searches were then ranked using Exomiser – a feature in GPAP – to generate a list of top candidates for each patient based on inheritance, variant strength, and how closely associated gene HPOs – if any – matched their phenotype[79]. These ranked variants were then manually investigated as described in section 2.1.2.1.

2.2 Morpholino Knockdown of Candidate CMS Genes in Zebrafish Embryos

2.2.1 Zebrafish Breeding and Maintenance

Adult zebrafish of an AB background and Casper lines of a Nacre background (obtained from Dalhousie University) were maintained by the Animal Care and Veterinary Services (ACVS) staff at the University of Ottawa in tanks of temperature (28.5°C) and pH-controlled water. Fish were fed twice a day with a mixture of pellet food and frozen blood worms to improve fertility and kept on a cycle of 14 hours light and 10 hours dark. All zebrafish breeding was done in accordance with protocols approved by the animal care committee (ACC) (protocol #: CHEOb-3169). Briefly,

1 male and 1 female fish were placed in a breeding tank with a mesh bottom insert and a removable barrier separating the 2 fish. Once their light cycle began, the barrier was removed to initiate pairing. Any eggs produced fell through the mesh bottom for collection and were filtered out with a fine mesh sieve. Embryos were then placed into a petri dish half full of blue water (0.01% methylene blue in system water) and separated into groups of no more than 30 per dish. All embryos were immediately used for morpholino (MO) microinjection or grown in a dark incubator at 28.5°C to no later than 168 hpf in accordance with ACC approved protocols (protocol #: CHEOe-3170). Euthanasia of embryos was accomplished by using a solution of blue water and tricaine methanesulfonate (4mg/ml) in a 1:1 ratio for 30min.

2.2.2 Morpholino Design

MOs were designed by Gene Tools LLC (USA) to block a splice site or the translational start site (TSS) of zebrafish orthologues *mgat5b* (exon 3/intron3 splice donor site – e3i3), *syt11a* (exon 2/intron 2 splice donor site – e2i2), and *syt11b* (e2i2) (Table 2-2). A fluorescent morpholino targeted to an intronic mutation in human beta-globulin (*HBB*) was used as a standard negative control (Gene Tools). A search of these sequences using NCBI's BLAST tool against the *Danio rerio* (assembly GRCz11) revealed no predicted off-target binding.

Gene	Transcript ID	MO Sequence (5'→3')	Target site
mgat5b	ENSDART00000182745.1	TGCACGCCATCTTACCTTCCACA	e3i3
mgat5b	ENSDART00000182745.1	ATGTGAAGGCTCTCCTCAACATTGC	TSS
syt11a	ENSDART00000080673.6	CAAGCTCATAAATGCTTACCTGTGT	e2i2
syt11a	ENSDART00000080673.6	ATTGGTCATCTCAGCCATTTTGGCG	TSS
syt11b	ENSDART00000078543.5	AATTGTTTGTGTTATCTTACCTGCA	e2i2
syt11b	ENSDART00000078543.5	CGATTTCGGTCATCTCAGCCATTTT	TSS
HBB	NA	CCTCTTACCTCAGTTACAATTTATA	NA

Table 2-2: All morpholino sequences and target sites. Morpholino sequences were designed using reference sequences found in Ensembl. The specific oligos, their target gene, and target sites (TSS = translation start site, e2i2 = exon 2/intron 2 border, e3i3 = exon 3/intron 3 boarder) are given in this table.

2.2.3 Morpholino Preparation

MOs were reconstituted with 100 µL of DPEC-treated water to a stock concentration of 3 mM and stored at -20°C. To prepare a 10 µl volume of final injection solution, an aliquot of MO was heated to 65°C for 10 min to dissolve any precipitated MO. Then, MOs were added to a final concentration of 0.5 mM in 1x Danieau's solution (58 mM NaCl, 0.7 mM KCl, 0.4 mM $MgSO_4*7H_2O$, 0.6 mM $Ca(Na_3)_2$ and 5 mM HEPES buffer) and 0.05% phenol red.

2.2.4 Morpholino Microinjection

Microinjection of zebrafish embryos with MOs against *MGAT5B* and *SYT11* zebrafish orthologues *mgat5b*, *syt11a*, and *syt11b* was accomplished by making micropipettes with filamented glass capillary tubes (Sutter Instrument Co., #BF100-50-10) and a needle puller (Sutter Instrument Co., Model: P-87; Parameters: Heat=590, Pull = 40, Vel = 50, Time = 150). Micropipettes were rear-loaded with 3 µl of MO solution (0.5 mM), placed in a micromanipulator, and their tips broken with fine-tipped forceps under a Leica MZ75 dissecting microscope. Dose calibration of each MO was accomplished by adjusting air pressure and time with a Narishige IM

300 Microinjector to deliver a consistent dose of MO with each injection. The following calculation was performed to find the required droplet diameter for each MO:

$$\text{Volume of a sphere} = V = \frac{4}{3}\pi r^3$$

Where *V* is the volume of a sphere in mm^3 (*V* mm) and *r* is the radius of the sphere in mm.

Assume 1 mm^3 = 1µl of MO solution at final concentration (FC) in mM.

Therefore, *V* mm^3 = *V*µl per injection

MO molecular weight (Mw) = MMw = 1 M

$$FC = \frac{MMw}{\left(\frac{1M}{FC}\right)}\text{g/L} = \left(\frac{\text{ng}}{\text{nl}}\right) * V\text{nl} = \text{ng of MO per drop}$$

Droplets were measured by injecting into oil placed on a micrometer. Once calibrated, zebrafish were paired as described in section 2.2.1. Collected embryos were then placed along the groves of a microinjection plate (Adaptive Science Tools, TU-1) made of 2% agar. Embryos were then rotated so the cell mass was away from the needle path. MOs were then injected into the embryo yolk sack behind the cell mass at the 1-4 cell stage. Injected embryos were stored in an incubator at 28.5°C until the appropriate time points were reached.

2.2.5 RNA Extraction and RT-PCR

Euthanized zebrafish were placed, 30 at a time, in 1.5ml tubes and liquid removed. Stainless steel beads and 600µl Buffer RLT from a RNeasy Mini kit (Qiagen) was added. Tubes were placed in to chilled TissueLyser (Qiagen) tube adaptors and lysed for 3 minutes at 25Hz. Steel beads were removed after lysis. Manufacturer instructions for the RNeasy Mini kit were then followed for isolation and purification of RNA. Concentration and purity of extractions were determined using a NanoDrop (ND-100 Spectrophotometer) then samples were stored

immediately at -80°C. RNA samples were used to synthesize cDNA according to manufacturer instructions (abm #G592) and used for expression studies and MO genotyping.

2.2.6 Primer Design and PCR for MO Knockdown Detection

Detection of zebrafish genes *magt5b* (ENSDART00000182745.1), *syt11a* (ENSDART00000080673.6) and *syt11b* (ENSDART00000078543.5) knockdown (KD) was accomplished with primers designed to detect expression of the native *mgat5b* transcripts and the retention of intron 2 in *syt11*a and *syt11b* as caused by the binding of MOs[80]. A search using NCBI's BLAST tool was performed for each primer against the zebrafish genome and found no off-target effects. PCR reactions were carried out using MyTaq™ DNA Polymerase in 20µl reactions with cDNA from 72 hpf zebrafish (RNA extraction and cDNA synthesis described in section 2.2.5) from embryos injected with splice-blocking (SB) MOs. Primers (Table 2-3) and thermocycler protocols (Table 2-4) can be found in the tables below. We used a standard thermocycler protocol for PCR with *mgat5b* primers and a touchdown protocol with all *syt11a/b* primers.

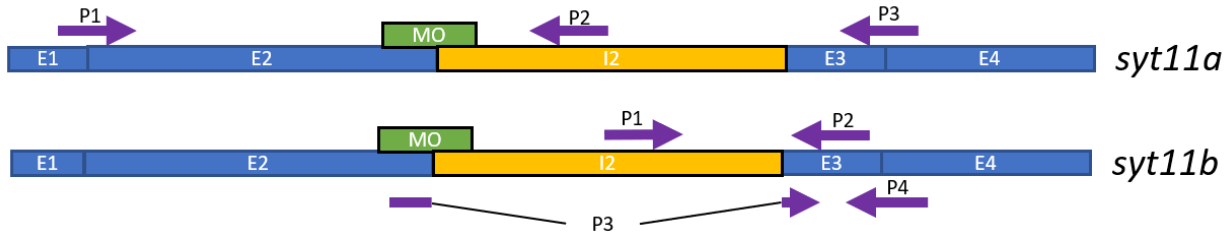

Figure 2.02 – Primer schematics for intron detection of *syt11a* and *syt11b*. The gene schematics for *syt11a* and *syt11b*. The morpholino (MO, green) binds to the splice donor site exon 2 and intron 2 causing retention of the latter in the final transcript and targeting it for degradation. Primers (purple arrows) look to amplify products specific to the native transcript or the intron 2 transcript.

Gene	Forward (5'→3')	Reverse (5'→3')	Product size (bp)
mgat5b	GGGCTACTGGAACCTCAACT	TCTTTGCCGTAAACCACAGC	158
	AACTGGGGCTACTGGAACCT	TGCAGGATGGAAAGCAATTT	209
syt11a	AGTGAGTGGACGAGTGAGTG	CTGGTGAAAGGCTCTGAGGA	195
	AACCAACCTATGATGTGTCC	GCTACACTATCCCACAATCC	945
		GAAGGTGTTTGGCCTTTAG	993
syt11b	CAGATCTCACGCTGCACTTC	AGAAACCAGCAGCTCTCCAT	178
	GTAACTACCAAGCGACCATT	GTGAGAAACAGGCTGATAGG	299
	AGAAACATGCAGTGTGTGAG	CGTAAGGATTTGCAGACAAGCC	145
ef1α	CTGGAGGCCAGCTCAAACATGG	CTTGCTGTCTCCAGCCACATTAC	

Table 2-3: Primer sets used for detection of MO knockdown.

Step	Temperature (°C)		Time	Cycles
	Regular	Touchdown		
Initial Denaturation	95	95	3min	1
Denaturation	95	95	15sec	30
Annealing	55	58-54 (-1 per cycle)	15sec	
Extension	72	72	30sec	
Final Extension	72	72	5min	1

Table 2-4: Standard PCR thermocycler protocol. Two different protocols were used for knockdown detection. The regular protocol for *mgat5b* and touchdown protocol for *syt11a* and *syt11b*.

2.3 Behavioural Assays

2.3.1 Spontaneous Chorion Activity Assay

Measurement of spontaneous chorion activity was done at 24 hpf with MO injected zebrafish embryos in blue water. We recorded their movements with a Leica EZ4 W at 25 fps for 1 min and saved the recordings as MP4 video files (Figure 2.03). Recordings were then imported in to Danioscope software (Noldus) for analysis. In Danioscope, each embryo was highlighted using the circle tool and tracked frame-by-frame to account for any drifting during recording. Activity threshold settings defining minimum parameters to be counted as a movement were set to 5% onset and 2% offset with a 10 ms minimum duration.

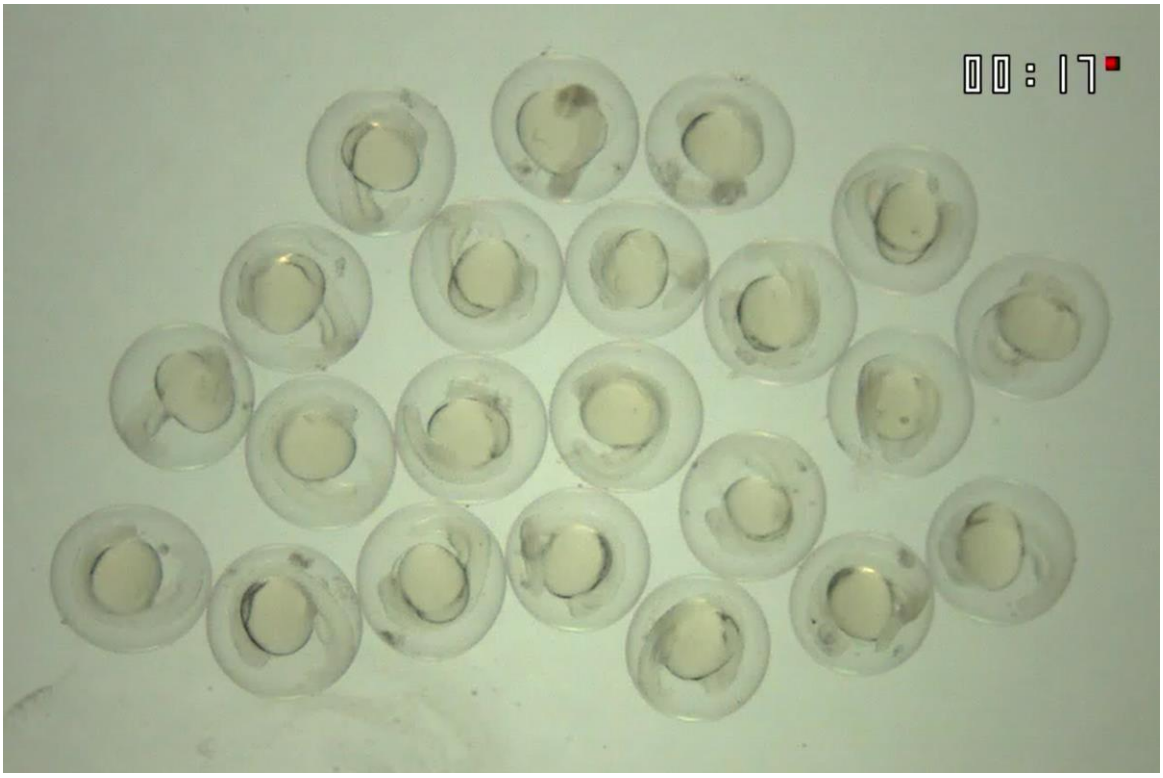

Figure 2.03 – Spontaneous chorion activity in 24 hpf zebrafish embryos. This figure depicts a representative image of a video recording taken for the measurement of zebrafish embryo activity inside the chorion.

2.3.2 Escape Response Assay

At 48 hpf embryos were enzymatically dechorionated with pronase (10 mg/ml) (Sigma) for 10 min in blue water. Once released from their chorions, fish were washed 3x with blue water. Embryos were then individually placed in a Petri dish with blue water and a Sony RX0 II (DSC-RX0M2) was placed 20 cm above the bottom of the Perti dish for optimal focus. A standard ruler with 1mm markings was placed in-frame so it could be used for scaling. Embryos were then stimulated with a gel-loading tip on the back of the head to elicit an escape response where the fish quickly swim in the opposite direction to the stimulus. This behaviour was recorded at 240 fps on a white background for maximal contrast to the zebrafish body. A recording apparatus was also constructed to eliminate recording artifacts like glare and shadows from lighting. Due to the high capture rate of the camera, all recordings were a maximum of 4 seconds in duration.

Video clips were imported as FFMPEG files into ImageJ for analysis with TrackMate software (Figure 2.04). Briefly, every video was cropped and trimmed to contain the whole movement of the embryo. A threshold to highlight the embryo as black spot on white background was set, then TrackMate was used to trace the movement.

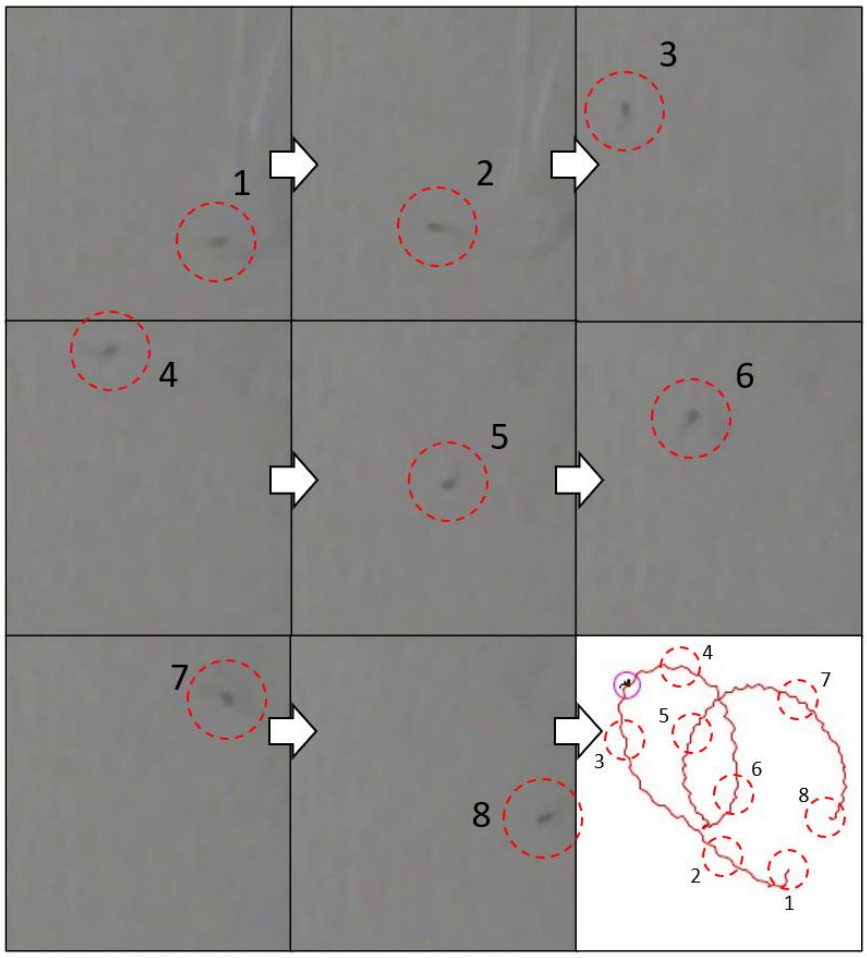

Figure 2.04 – Escape response trace. The panels in this figure represent frames pulled from a video recording of a zebrafish escape response. Each circle highlights the position of the embryo throughout the movement. The last panel (bottom right) is a complete trace as generated by TrackMate with the positions of the fish in each pulled frame (labelled 1-8 respectively).

2.4.2.1 Automated Analysis of Escape Response Data from TrackMate

To reduce error and speed up analysis of the escape response assay we developed a script using python to extract and calculate total distance, average velocity, and acceleration from each comma-separated values (CSV) file outputted by TrackMate. In brief, the code searches each file looking for displacement and velocity data. Then looks for increases in velocity over time, finds the difference between the two points, then uses the recording rate of the camera in frames per second (FPS=240), divided by the number of frames the increase in velocity lasted, to calculate every acceleration throughout the movement of the fish. The generalized equation is found below where A = acceleration in mm/s^2, V_1 = initial velocity in mm/s, V_2 = final velocity in mm/s, FPS = frame rate of camera, and # of frames = the number of frames of sequential velocity increase:

$$A\ \mathrm{mm/s^2} = \frac{(V_2 - V_1) * \mathrm{FPS}}{\#\ \mathrm{of\ frames}}$$

It then generates two .CSV files named: “accelerations.csv” and “averages.csv”. The accelerations file gives all the accelerations calculated from each movement and labels which file it was from. Then the “averages” file generates another .CSV listing the total distance travelled and average velocity throughout the movement of each fish. The source code for this process is found Appendix I.

2.4 Imaging

2.4.1 Morphology

Images of zebrafish embryos were taken at 48 hpf with a Leica EZ4W microscope. Fish were anesthetized with tricaine (100 mg/L in blue water) to immobilize them while imaging. Then images were taken at 8X zoom, to measure body length, eye size and cardiac area using Danioscope. Images were also taken for scale calibration by taking photos of the markings of a ruler at the same zoom level as the photos of the fish.

2.4.2 Immunological Staining

For immunological staining we used Casper zebrafish which lack pigmentation for better imaging. Embryos were dechorionated with pronase, as described in section 2.3.2, and euthanized with tricaine as described in section 2.2.1 at different timepoints between 24-72 hpf. Embryos were then fixed overnight in 4% paraformaldehyde (PFA) in phosphate buffered saline (PBS) followed by a 10 min wash in dH_2O. Any embryos >48 hpf were treated with collagenase A (Milipore Sigma, 1 mg/ml, 72 hpf = 30 min treatment) then washed for 10 min in PBS. All embryos were then permeabilized for 7 min in 100% ice cold acetone, immediately washed 2x for 5 min in PBS, then blocked with 5% horse serum (HS) in 0.1% PBS-Tween (PBST) at room temperature for 1 hour. This was followed by incubation with a synaptic vesicle protein 2 (SV2) antibody (DSHB, 1:500 in 5% HS in PBST) overnight at 4°C. The embryos were then washed 5x in PBST and incubated in α-Bungarotoxin, Alexa Fluor™ conjugate (Invitrogen B13422, 1:1000) and 594 Alexa Fluor™ goat anti-mouse IgG1 antibody (Invitrogen A21125, 1:200) for 2 hours at room temperature, washed 2x in PBST for 20 min, and washed overnight at 4°C in PBST. Embryos were mounted on microscope slides with layered, windowed electrical tape filled with Vectashield mounting medium (Vector Laboratories) and sealed with nail varnish and a #1.5 coverslip. Z-

stacks of stained embryos were obtained with an Olympus Fluoview FV-1000 Laser Confocal Microscope under the 20X objective lens. Imaging parameters were held constant between fish.

2.4.3 Image Preparation and Analysis

Raw confocal z-stack images were prepped for colocalization analysis by using the ImageJ polygon tool to define specific regions of interest (ROIs) and to eliminate unrelated biological structures (i.e., spinal cord), noise, and background from the images that would otherwise interfere with analysis. These images were then subject to a Pearson's statistical test using the ImageJ plugin, Coloc 2.

Maximum intensity projections of all z-stacks files were then generated keeping the channels separate. Using the polygon tool, myotomes were traced one-by-one in the AChR channel (green) and measured for total area (Figure 2.05). Each total area was then subtracted from the last to get the individual area of each myotome in the image as in the calculation below:

$$M_1 = A_1,$$
$$M_2 = A_2 - A_1,$$
$$M_3 = A_3 - A_2,\ldots$$
$$M_n = A_n - A_{n-1}$$

Where M_n is the individual myotome area and A_n is the total area output given by ImageJ each time a new myotome was traced. The selection of each image was then inverted to select everything but the traced myotomes in both the AChR and SV2 channel (red) then removed to eliminate any excess myoseptal staining. Noise was removed by thresholding the image and using the de-speckle tool. The area of each dot left represented presynaptic (SV2) and postsynaptic (AChRs) staining. These spots were then measured for their total area and using the "analyze particles" option in ImageJ. Neuron length was measured in the SV2 (red) channel using the

freehand line tool and tracing the length of the neuron from the spinal cord down the axon and up the "j-loop" of myoseptal innervation.

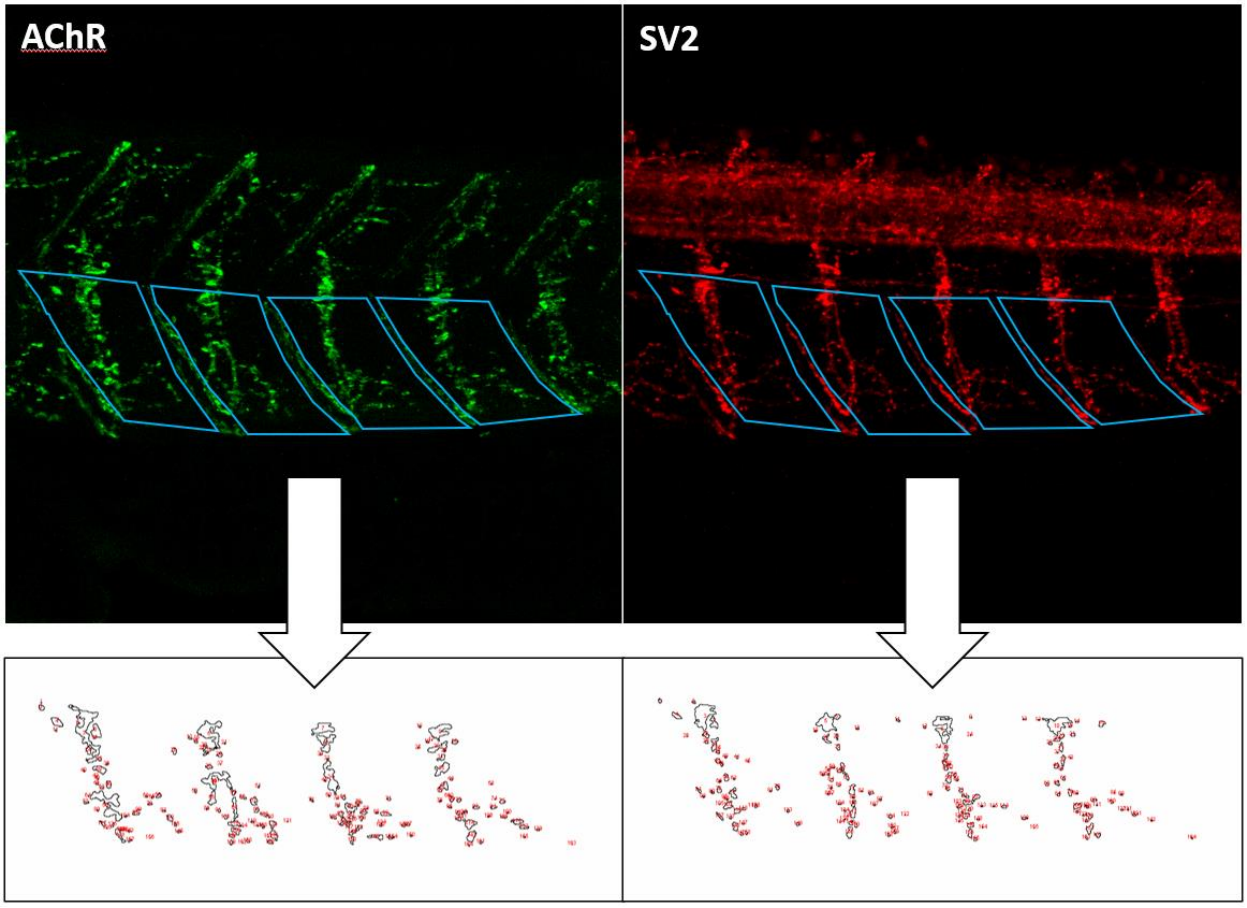

Figure 2.05 – ImageJ analysis of zebrafish neuromuscular developmental features. Zebrafish postsynaptic AChRs stained with 488-conjugated α-BT (green) and motor neuron axons stained with SV2 (red) are shown in the top 2 labeled panels. The regions of interest (ROIs) highlighted in blue are the defined myotomes and were used for both colocalization analysis and spot analysis defining the area of pre- and postsynaptic NMJ structures. The bottom panels are the output maps generated with ImageJ highlighting the areas included in these measurements.

2.5 Statistics

All statistics between groups of control MO injected trials and knockdown MO injected trials were first checked for normality using Anderson-Darling, D'Agostino & Pearson, Shapiro-Wilk, and Kolmogorov-Smirnov tests. If the data sets failed any one of these tests, a non-parametric Mann Whitney test was used to test for significance because the groups to be compared were independent from each other and the distribution was not normal. All non-symmetrical datasets are represented as median (inter quartile range; sample size). If a data set passed all normality checks, an unpaired t-test was done to calculate significant difference. Symmetrical datasets are shown as mean (SD). All experiments compared controls to their corresponding knockdown clutch mates. Results showing $P<0.05$ were considered statistically significantly different.

3. Results

3.1 Exome Analysis of 2 CMS Cohorts Reveals New Diagnosis and Novel CMS Gene Candidates for *in vivo* Study

Primary and secondary exome analysis results from Cohort 1 solved 12 cases with variants in canonical CMS genes *CHAT, CHRNE, CHRND, MUSK, AGRN, GFPT1* and *DPAGT1* (Figure 3.02). Of these cases, secondary exome analysis provided new genetic diagnosis for 7 patients (Table 3-1). The proportion of solved cases in cohort 1 was greater in those cases where DNA sequences of at least 1 other relative was provided (sib pairs = 50%, families of 4 = 100%, trios = 27%, and duos = 40%, Figure 3.01). In total, cohort 1 solved 14 cases, has 13 ongoing cases (requiring parental DNA or further clinical investigation), and 21 cases yet to be solved. Secondary analysis of cohort 2 solved 5 of 23 cases with variants in *CHAT, CHRNE, RAPSN, LMOD3,* and *SYT2* (Figure 3.02 & Table 3-1). All cases in cohort 2 were singleton cases and had a similar distribution of solved (22%), ongoing (17%), and unsolved (61%) cases as compared to the distribution of singleton cases in cohort 1. The vast proportion of solved cases were solved with canonical CMS genes. In cases with variants of unknown significance (VUS), variants can come from any gene, including canonical CMS genes but these may require identification of a second cryptic variant or a further segregation analysis with parental sequences to confirm diagnosis.

Cases with variants of unknown significance (VUS) were also uncovered during analysis (Table 3-2). These VUS require further investigation by clinicians or researchers to determine whether they are causative of the patient's phenotype. It is from this pool of variants that we identified 2 genes; *MGAT5B* and *SYT11,* for further investigation *in vivo*.

Patient 35 harbored a homozygous mutation in *MGAT5B* (see Table 3-2) that was only uncovered through relaxation of allele frequency (AF) parameters from <0.001 to <0.01 (*MGAT5B*

variant AF = 0.0010001). Analysis of this patient using the primary filtering techniques described in section 2.1.2.1 yielded too large a list for manual analysis (Table 3-3). Therefore, the Exomiser tool was used to prioritize and eliminate many of them from contention, leaving *MBGAT5B*, among others, as primary candidates (Table 3-3) Primary analysis of patient 65 with standard filtering (section 2.1.2.1) revealed a homozygous (hom.) variant in *SYT11*. Further database-wide searches found a second heterozygous (het.) in patient 101, a member of cohort 2.

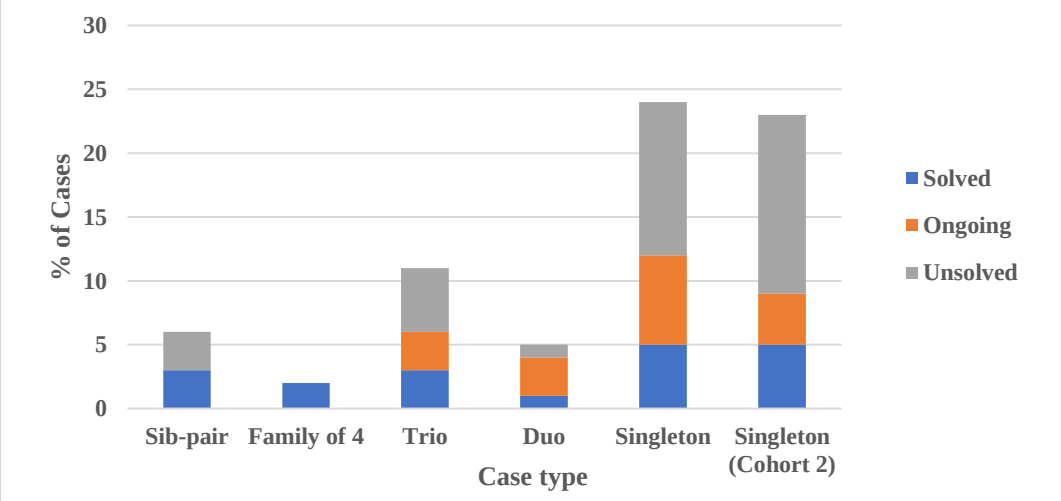

Figure 3.01 – Case status proportions of cohort 1 and cohort 2. Solved cases (blue) have been confirmed by clinicians and tagged as pathogenic in GPAP. Ongoing cases are those which require further investigation, often needing more information about patient phenotype or the DNA from a parent to confirm inheritance.

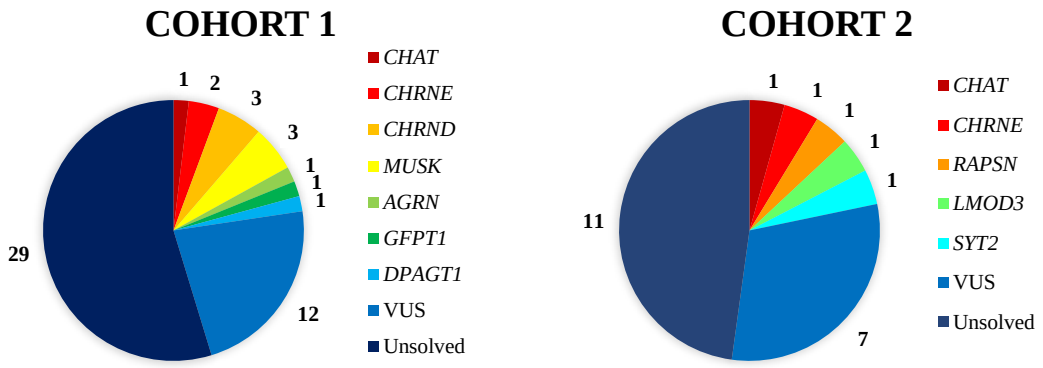

Figure 3.02 – Total cases solved with canonical CMS genes. The chart on the left shows the proportion of cases from cohort 1 solved with canonical CMS genes, to variants of unsolved significance (VUS), to cases that remain unsolved with no candidates for investigation. The chart on the right shows the same information for cohort 2.

Patient #	Gene	Zygosity	Allele 1	Allele 2	Amino acid change(s)	
6	*GFPT1*	c.het.	c.*22C>A	c.365A>G	3' UTR	p.His122Arg
20	*CHRNE*	hom.	c.1353dupG		p.Asn452GlufsTer4	
45	*CACNA1S*	het.	c.2689A>G	-	p.Arg897Gly	-
52	*MUSK*	hom.	c.1742T>A		p.Ile581Asn	
74	*ANO5*	hom.	c.191dupA		p.Asn64LysfsTer15	
75	*ACTA1*	het.	c.289C>T	-	p.Arg97Cys	-
81	*PURA*	het.	c.581G>A	-	p.Gly194Glu	-
95	*CHAT*	hom.	c.1840-9A>G c.1282-183G>A	c.1840-9A>G c.1282-183G>A	intronic intronic	
100	*LMOD3*	hom.	c.138_139insC		p.Ser47GlnfsTer13	
102	*RAPSN*	c.het.	c.1119_1121delNNN	c.677N>A	p.Lys373del	p.Met226Lys
108	*CHRNE*	c.het.	c.422N>T	c.103N>C	p.Pro141Leu	p.Tyr35His
110	*SYT2*	het.	c.903C>A	-	p.Asp301Glu	-

Table 3-1. Newly solved cases and respective variants. This table highlights the exact position of variants uncovered during primary and secondary exome analysis which were used to solve each case. Segregation of each variant was either confirmed in the case of heterozygous (het.) and compound heterozygous (c.het) variants, or highly likely in the case of homozygous (hom.) variants – which are considered solved, but parental sequencing is needed for segregation.

Patient #	Gene	Zygosity	Allele 1	Allele 2	Amino acid change(s)	
8	*CHRND*	het.	c.1315G>A	-	p.Val439Met	-
12	*KIF21A*	het.	c.2860C>T	-	p.Arg954Trp	-
14	*KBTBD13*	het.	c.31G>A	-	p.Val11Met	-
19	*GPAT2*	hom.	c.2225A>C		p.Asp742Ala	
29	*CHRND*	het.	c.79C>T	-	p.Arg27Trp	-
30	*CHRND*	het.	c.769T>C	-	p.Cys257Arg	-
	TRPV4	het.	c.760G>A	-	p.Val254Met	-
31	*NEB*	c.het.	c.6817A>G	c.2923G>A	p.Lys2273Glu	p.Ala975Thr
	COL6A3	het.	c.1906A>G	-	p.Asn636Asp	-
32	*MBNL3*	hom.	c.922T>C		p.Phe308Leu	
	COL6A2	het.	c.289G>A	-	p.Gly97Ser	-
36	*ABCC8*	het.	c.4256G>A	-	p.Arg1419His	-
	FOXRED1	het.	c.632G>C	-	p.Gly211Ala	-
34	*HSPG2*	c.het.	c.8370A>C	c.3346G>A	p.Glu2790Asp	p.Gly1116Ser
35*	*MGAT5B*	hom.	c.868A>G		p.Ile290Val	
43	*NEB*	c.het.	c.24056C>T	c.8994+32G>A	p.Pro8019Leu	intronic
65*	*SYT11*	hom.	c.55G>A		p.Gly19Ser	
	CHRND	het.	c.727C>T	-	p.Arg243Cys	-
66	*MUSK*	het.	c.2401C>T	-	p.Gln801Ter	-
	TTC19	hom.	c.-227C>A		5' UTR	
71	*CLCN1*	het.	c.501C>G	-	p.Phe167Leu	-
	CSMD2	c.het.	c.4882G>A	c.2062C>T	p.Gly1628Arg	p.His688Tyr
	MFAP4	c.het.	c.433G>A	c.263G>A	p.Ala145Thr	p.Gly88Asp
84	*SPR*	het.	c.751A>T	-	p.Lys251Ter	-
85	*TPP1*	het.	c.622C>T	-	p.Arg208Ter	-
89	*TCOF1*	het.	c.256G>A	-	p.Glu86Lys	-
90	*UNC13B*	het.	c.2023T>G	-	p.Ser675Ala	-
92	*SYNE2*	het.	c.20134G>A	-	p.Glu6712Lys	-
101*	*SYT11*	het.	c.949C>T	-	p.His317Tyr	-

Table 3-2. Patients with variants of unknown significance. The variants shown here are currently under investigation for potential pathogenicity in their respective patients. Typically, in cases which are singletons, parental DNA is needed for segregation analysis, which is the case for many of the patients with heterozygous (het.) variants in canonical CMS genes or homozygous/compound heterozygous (hom./c.het.) variants which are in non-CMS genes. Starred (*) patients are those with particularly interesting variants that are linked to pathways known to work at the NMJ and have been flagged as candidates for *in vivo* zebrafish study.

Patient #	Total coding variants	Total rare variants	Total rare variants after HPO gene lists	Exomiser prioritized genes	Candidates after manual investigation
35	103140	4015	69	*RYR1* (2 het.) *DST* (3 het.) *UNC80* (2 het.) *TG* (2 het.) *ATXN3* (2 het.) *FAT2* (2 het.) *MGAT5B* (hom.)	*MGAT5B* (hom.)
65	106892	3211	44	*ARMC9* (2 het.) *MARS1* (hom.) *NAGLU* (hom.) *AHNAK2* (2 het.) *SYT11* (hom.) *ACOT2* (het.)	*SYT11* (hom.)
101	189047	4772	27	*LMNA* (2 het.) *ATXN1* (2 het.) *ATXN7* (het.) * *MYBPC3* (het.) * *ATXN3* (het.) * *TECPR2* (het.) * *SYT11* (het.) * *FAM134B* (het.) * *DNAH17* (het.) *	*SYT11* (het.)

Table 3-3. Exome analysis reveals *MGAT5B* and *SYT11* as primary candidates for CMS. The three patients in this table showed interesting variants upon analysis of their exomes. The number of variants upon initial filtering based on allele frequency (rare variants) and then targeted searches with human phenotype ontology (HPO) terms. All targeted lists were further filtered by using Exomiser to rank and eliminate variants based on inheritance, variant strength (high, moderate, low, modifier), and similarity to patient phenotype.

3.2 *MGAT5B* and *SYT11* are Novel CMS Gene Candidates

3.2.1 Patient 35 Harbours a Rare Variant in the Glycosylation Gene *MGAT5B*

Patient 35 is a singleton female case in cohort 1 with infantile onset CMS and presented with ptosis, respiratory insufficiency, and fatigable muscle weakness of the proximal muscles (Table 3-4) harbouring a homozygous *MGAT5B* variant (c.868A>G; p.Ile290Val) in exon 8 of the main transcript (ENST00000569840.6) (Table 3-4). This variant was found to have an allele frequency of 0.0010001 in the gnomAD database, which just exceeded primary filtering thresholds (AF = <0.001).

Patient #	Phenotype (HPOs)	Gene	Gene Constraint (o/e)	Mutation	AA Change
35	Ptosis Reduced tendon reflexes Muscle weakness Dysphagia Respiratory insufficiency due to muscle weakness Fatigable weakness Proximal muscle weakness Exercise-induced muscle fatigue	*MGAT5B*	0.47	c.868A>G	p.Ile290Val

Table 3-4. Phenotype of CMS patient with candidate CMS gene *MGAT5B*. Patient 35 was found to have a rare variant in *MGAT5B*, a gene with a genetic constraint of <1 (o/e = observed over expected where >1 means a protein is predicted to tolerate variants and still function).

As a way to establish potential links to known CMS genes, we used GeneMANIA to create an integrated network of genetic and protein interactions based on common pathways, co-expression/localization patterns, protein homology, physical/genetic interactions and other proteins within one degree of separation between *MGAT5B* and known pre- and postsynaptic CMS genes (Figure 3.03)[77]. This interaction network revealed *MGAT5B* is co-expressed with the syntaxin genes *STX1A* and *STX1B* and has genetic interaction with *MYO9A* (Figure 3.03). The syntaxins are a group of genes that code for vesicle fusion/trafficking proteins in eukaryotic cells and include SNARE and SNAP proteins, of which *SNAP25* is a known CMS gene [55,81]. The genetic interaction between *MYO9A* and *MGAT5B* is also interesting as *MYO9A* is a CMS gene that participates in neurite branching and secretion of the highly glycosylated signalling peptide agrin[67,82,83]. Of the postsynaptic CMS genes, *MGAT5B* is only predicted – with very low confidence – to be co-expressed with *CHAT* [84].

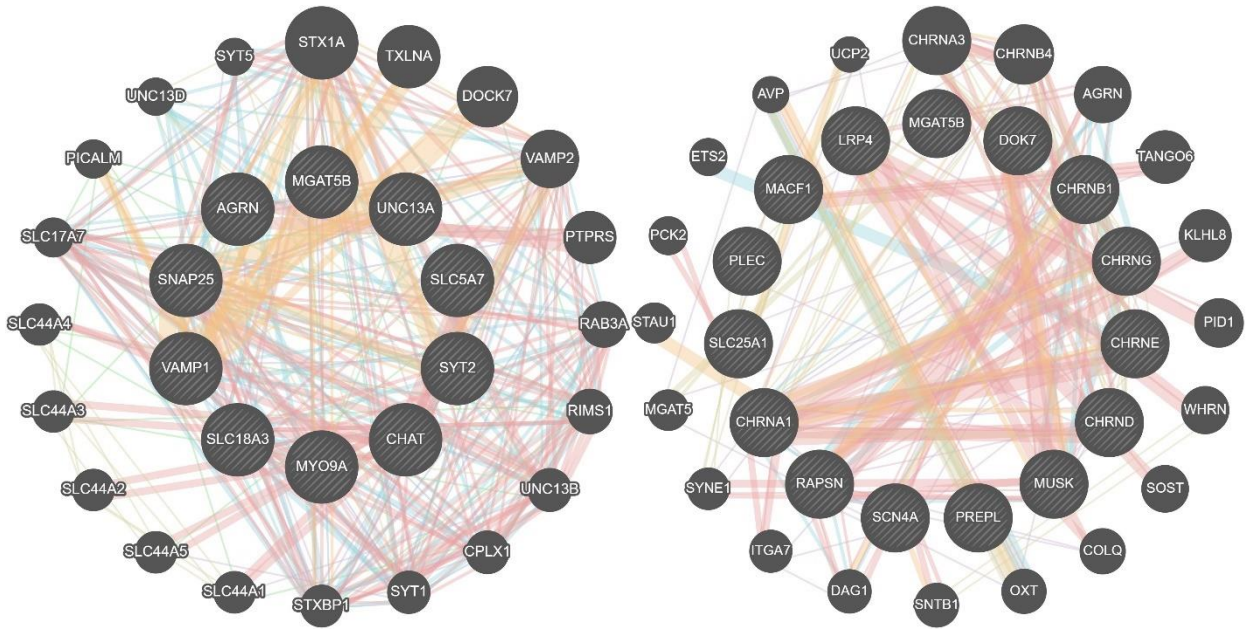

Figure 3.03 – Protein interaction networks of pre- and postsynaptic CMS genes with *MGAT5B*. These interaction networks show that *MGAT5B* interacts with presynaptic CMS genes (left) and less with postsynaptic genes (right). The thickness of the lines between nodes (genes) represents the strength of their relationship and the colour represents the type of relationship; common pathways (blue), co-expression (purple), co-localization (violet) protein homology (yellow), physical (pink), genetic (green), and predicted interactions (orange).

3.2.2 Morpholino Knockdown of Zebrafish *mgat5b* Shows No Neuromuscular Deficiency

To determine if *MGAT5B* is a novel CMS gene we utilized a morpholino zebrafish model (section 2.3.5) to induce transient knockdown of the *MGAT5B* zebrafish orthologue *mgat5b*. We looked at wild type zebrafish expression of *mgat5b* over the first 7 days of development and confirmed MO knockdown by RT-PCR (Figure 3.04). Results show that *mgat5b* is expressed over the first 7 days of development and that MO knockdown with a 2ng dose at the 1-4 cell stage is sufficient to reduce *mgat5b* transcript expression at 72 hours post fertilization (hpf) (Figure 3.04)[65,67,85,86]. We then measured locomotor development in *mgat5b* morphants by recording spontaneous chorion movements and their response to touch (escape response). *mgat5b* morphants showed an increase in activity rate (bursts/minute) of ~30% at 24 hpf as compared to control MO injected clutch mates (Figure 3.05). Peak activity usually occurs at around 19 hpf and declines until about 26 hpf[63]. Therefore, the increase observed in *mgat5b* morphants could have been caused

by a shift in peak chorion activity due to a delay in neuromuscular development. With this in mind, we recorded *mgat5b* morphant activity at 24, 26, 28, and 30 hpf in search of an eventual decline in activity. As previously found, embryos at 24 hpf showed a significant increase (~98%) over their respective controls (Figure 3.06). This increase was also seen to be significant up to 28 hpf – at 30 hpf the embryos returned to control rates of activity (Figure 3.06). The general decline in activity from 24-30 hpf suggests that *mgat5b* knockdown causes a delay in neuromuscular development which shifts peak activity from 19 hpf [13] to about 24 hpf (Figure 3.06).

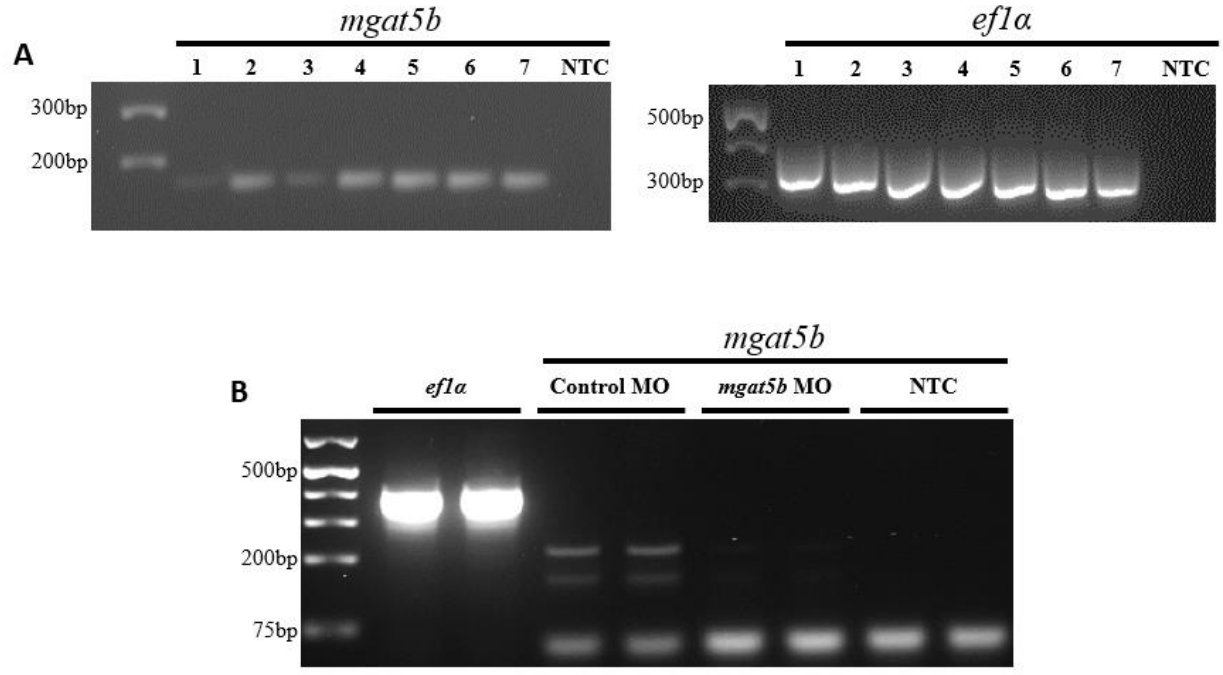

Figure 3.04 – Developmental expression and morpholino knockdown of *mgat5b*. (A) RT-PCR was used confirm *mgat5b* expression over the first 7 days of zebrafish embryonic development. The same cDNA samples were used for both the right (*mgat5b*) and left (*ef1α* positive controls). PCR reactions for both images were conducted with the same cDNA samples but on different gels as they were also used as positive controls to detect *syt11a* and *syt11b* expression (Figure 3.20) (B) Morpholino knockdown of *mgat5b* in 72 hpf embryos caused by retention of intron 4 is seen by the loss of transcript expression in the MO injected fish.

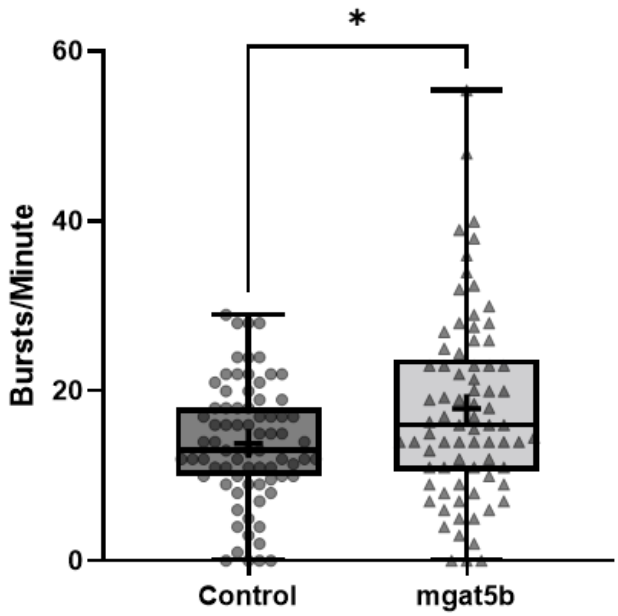

Figure 3.05 – Spontaneous chorion activity of zebrafish embryos at 24 hpf is increased on knockdown of *mgat5b*. The knockdown of *mgat5b* in zebrafish increased spontaneous movement from 12.99 bursts/min (9.99, 18.01; *n* = 75) in the controls to 15.98 bursts/min (10.49, 23.70; *n* = 77) in the knockdown (Mann Whitney test, **P<0.05*).

A

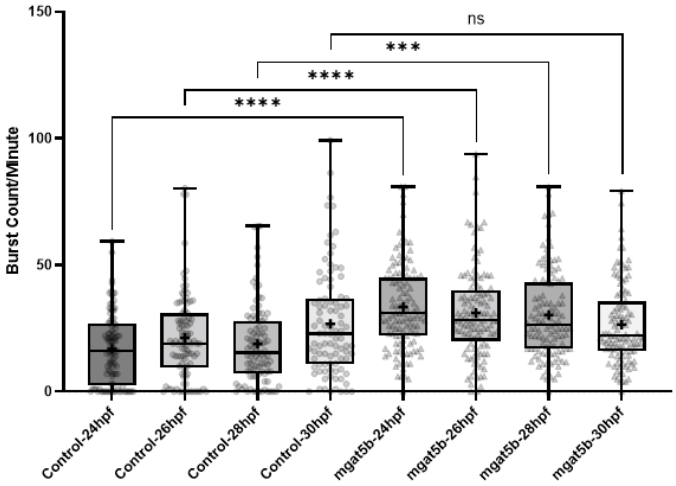

B

	Mean Activity Rate (bursts/min)	
Time	Control (*n* = 100)	*mgat5b* (*n* = 121)
24 hpf	15.98 (2.25, 26.86)	30.97 (21.98, 45.17)
26 hpf	19.48 (9.60, 30.97)	28.30 (19.98, 39.96)
28 hpf	16.98 (7.99, 29.71)	27.97 (16.98, 45.96)
30 hpf	23.94 (11.49, 44.66)	22.98 (16.37, 40.10)

Figure 3.06 - Chorion activity rate of 24-30 hpf *mgat5b*-KD embryos returns to control levels after 28 hpf. The movement of control and *mgat5b* MO injected zebrafish embryos were recorded for 1 minute at 25 fps with a Leica EZ4W stereomicroscope at 24, 26, 28, and 30 hpf. (A) Significant increase in burst rate between control and *mgat5b*-SB knockdown embryos from 24-30 hpf and a return to control levels of movement at 30 hpf were observed (Mann Whitney test, ns = not significant, *****P<0.0001*, ****P<0.001*). (B) Summary of activity rate in bursts/minute, all values are shown as median (25% and 75% quartiles), SB = splice-blocking morpholino.

Touch response assays were also conducted at 48 hpf to measure later markers of locomotor development, namely the fish's ability to accelerate – which is a measure of muscle contractile force[63]. Responsiveness to physical stimulus in *mgat5b* morphants was not altered compared to controls (Figure 3.07). When morphants did respond, no difference was found in total distance travelled, average velocity, or initial acceleration of their movements, indicating there is no neuromuscular deficit in these *mgat5b* fish (Figure 3.07).

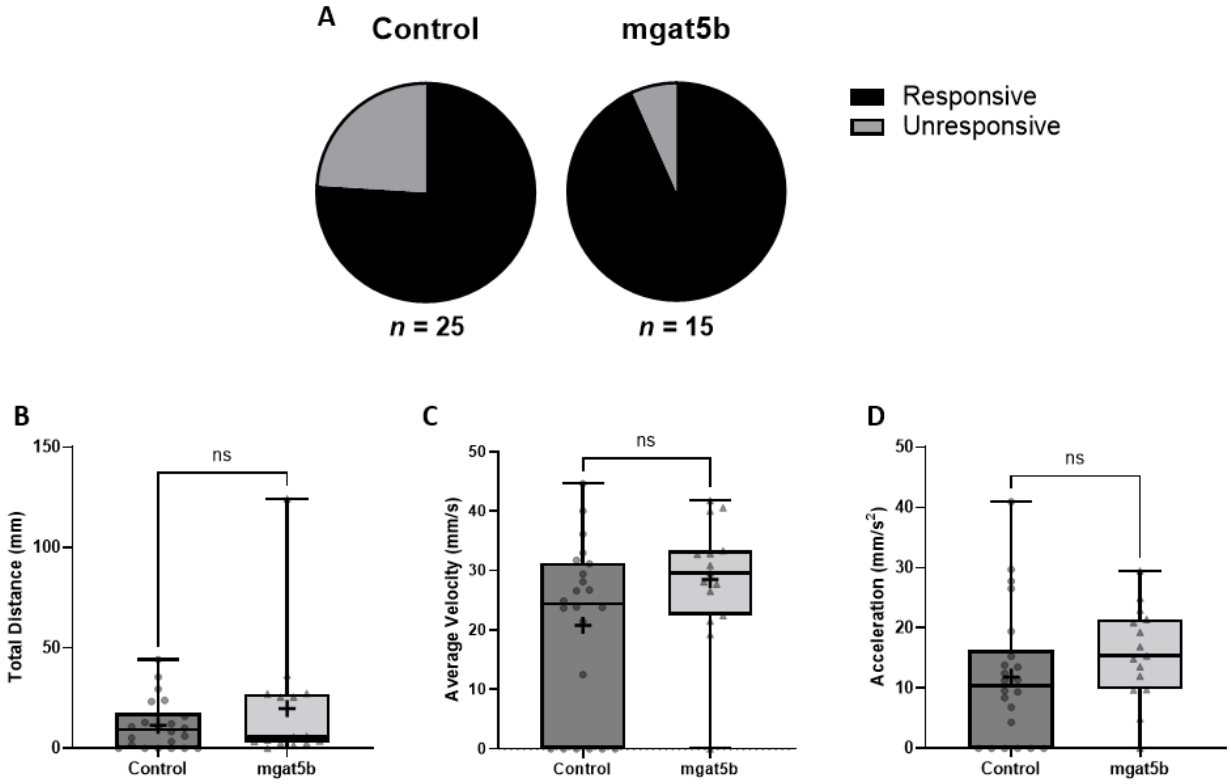

Figure 3.07 - Escape response measurements of 48 hpf *mgat5b*-KD zebrafish embryos. (A) Escape response was evoked in 19/25 control and 14/15 *mgat5b*-SB MO injected embryos. (B) There was no significant difference found in the total distance (Control = 9.24 mm (0, 17.78), *mgat5b* = 5.67 mm (2.86, 27.19); Mann-Whitney test), (C) average velocity (Control = 24.38 mm/s (0, 31.29), *mgat5b* = 29.61 mm/s (22.45, 33.30); Mann-Whitney test), or (D) initial acceleration (Control = 10.44 mm/s^2 (0, 16.34), *mgat5b* = 15.36 mm/s^2 (9.76, 21.42); Mann-Whitney test) when comparing control to morphant fish. Control *n* = 25, *mgat5b n* = 15, ns = not significant.

We continued *mgat5b* developmental studies with immunological staining of *mgat5b* knockdown casper zebrafish (pigment-free fish) using an antibody against synaptic vesicle protein 2 (SV2) and fluorescently labelled α-bungarotoxin (α-BT) to mark motor neurons and postsynaptic

acetylcholine receptors (AChRs) respectively[65,67]. This allowed us to determine the state of neuromuscular development in 48 and 96 hpf *mgat5b* knockdown embryos by calculating the degree of colocalization of these two markers (Figure 3.08). Using Pearson's coefficient, where 1 represents perfect colocalization, and -1 perfect anti-colocalization, we determined no significant difference in colocalization of SV2 and AChRs at 48 hpf (Figure 3.08). Some anomalies were noted in the migration and branching patterns of motor neuron axons in *mgat5b* embryos at 48 hpf where myoseptal innervation seems less organized with branches in the opposite direction as compared to the traditional j-loop migration pattern innervating the myosepta of control embryos [13,14]. This abnormal branching pattern appears to correct itself by 96 hpf. Interestingly, at 96 hpf there is a significant increase in colocalization in *mgat5b* fish as compared to controls (Figure 3.08).

Although there are differences seen in chorion activity and early motor neuron axon branching patterns which could represent a delay in neuromuscular development, the return to control levels of activity at 30 hpf (Figure 3.06) and increase in myotome innervation at 96 hpf (Figure 3.08) suggest that knockdown of *mgat5b* is not sufficient to cause a sustained neuromuscular deficit – as would be expected of a gene that causes CMS.

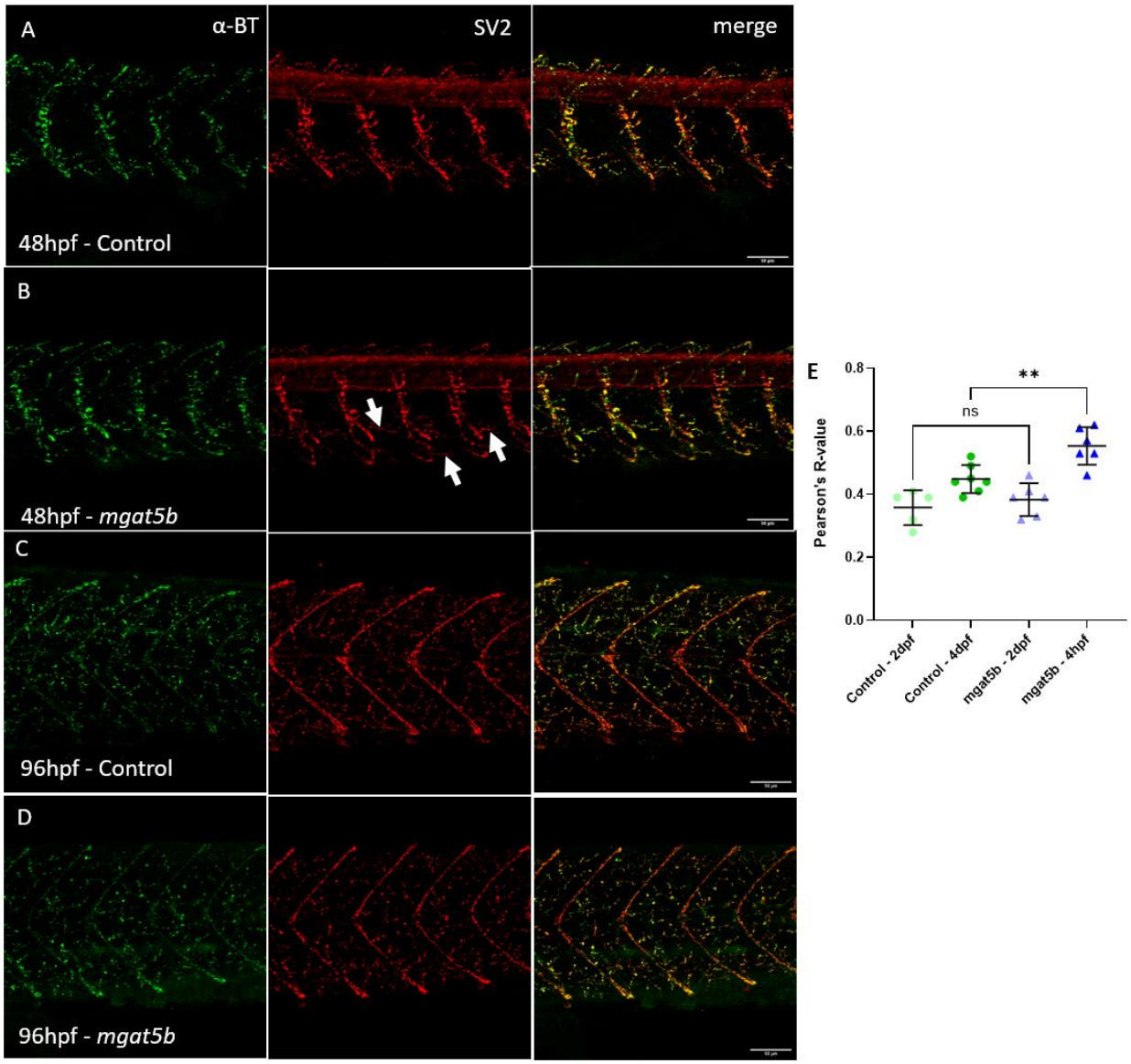

Figure 3.08 – Progression of neuromuscular innervation in 48 and 96 hpf *mgat5b* morphant casper zebrafish. (A) Control and (B) *mgat5b* morphants stained for AChRs (green) and SV2 (red) show abnormal organization of motor neuron axons (arrows) branching from the spinal cord. (C & D) morphants at 96 hpf show similar axon branching patterns as compared to their controls. (E) At 48hpf *mgat5b*-SB knockdown embryos show no significant difference in colocalization of AChRs and SV2 (Control - 48 hpf = 0.36 (0.055), *n* = 5; *mgat5b* – 48 hpf = 0.38 (0.052), *n* = 6; unpaired t-test, ns = not significant). Increased degree of colocalization representing myotome innervation is seen in *mgat5b* morphants at 96hpf (Control = 0.45 (0.045), *n* = 7; *mgat5b* = 0.55 (0.060), *n* = 7; unpaired t-test, ***P<0.01*). Values are mean (SD). Scale bar = 50 μm.

3.2.3 Patients 65 and 101 Contain Rare Variants in the Vesicle-trafficking Gene *SYT11*

Two unrelated cases were found to possess variants in *SYT11* (Table 3-5). The first case was from cohort 1 and is a singleton female from a consanguineous family with ptosis, fatigable weakness, and a decremental response to repetitive nerve stimulation (Table 3-5). The *SYT11* variant found in this patient is a homozygous c.55G>A causing p.Gly19Ser and has an allele frequency of 0.0049 with 14 heterozygous and 0 homozygous people found in gnomAD. The variant is located in exon 2 of the primary transcript (ENSMUST00000107505.7) in an area coding for a transmembrane region (TMR) highly conserved across synaptotagmin proteins[87]. This singleton case is known to have two healthy parents and a possibly affected nephew. With this inheritance pattern in the family, it is highly likely the causative variant follows recessive inheritance patterns consistent with this homozygous *SYT11* variant (Figure 3.09). So far, we have been unable to study any relatives of patient 65 genetically. The second case is a singleton male, who's parents were not available for study, from cohort 2 with respiratory insufficiency, fatigable proximal muscle weakness and scapular winging. When a database-wide search was conducted for other patients with *SYT11* variants it was revealed that patient 101 contained a heterozygous c.949C>T resulting in p.His317Tyr in *SYT11*. This variant has an allele frequency of 0.000016 with 4 heterozygous and 0 homozygous people found in gnomAD. The position of this variant is in exon 3, a part of the primary transcript coding for the second of 2 highly conserved synaptotagmin C2 domains known as C2A and C2B. Together, C2A and C2B can bind up to 5 Ca^{2+} cations between them, depending on the type of synaptotagmin[87,88]. The variants from both cases have the potential to alter *SYT11* splicing through activation of an exonic cryptic acceptor site and alteration of an exonic splicing enhancer site respectively[76].

Patient #	Phenotype (HPOs)	Gene	Gene Constraint (o/e)	Mutation	AA Change
65	Ptosis EMG: decremental response Fatigable weakness	*SYT11*	0.37	c.55G>A	p.Gly19Ser
101	Respiratory insufficiency due to muscle weakness Fatigable weakness Scapular winging Proximal muscle weakness	*SYT11*	0.37	c.949C>T	p.His317Tyr

Table 3-5. Phenotypes of CMS patients with candidate CMS gene *SYT11*. Patients all showed fatigable weakness in their muscles. Rare homozygous and heterozygous variants in *SYT11* were found in patients 65 and 101. *SYT11* also has a very low tolerance for mutation as its genetic constraint is <1.

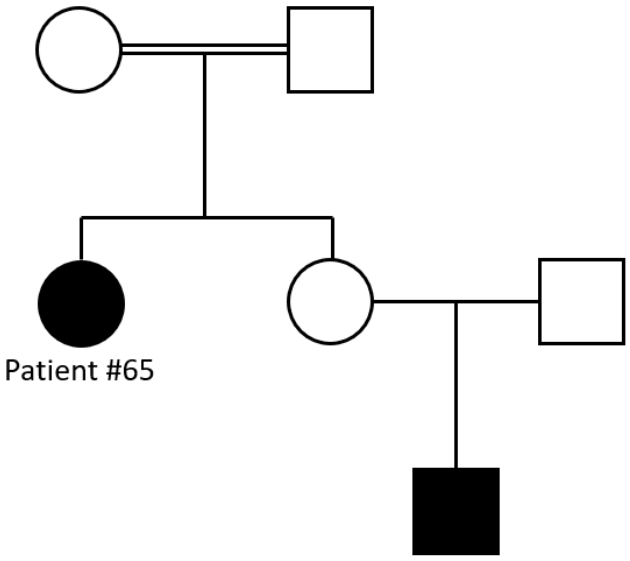

Figure 3.09 – Patient 65 family pedigree. This figure shows the family tree of patient 65 where all the circles are females, squares are males, and shaded individuals are affected with CMS.

Using the same approach as with *MGAT5B*, an interaction network of pre- and postsynaptic CMS genes with *SYT11* was generated using GeneMANIA (Figure 3.10). *SYT11* showed potential co-expression with *SNAP25* – another vesicle trafficking known to CMS. There is also a predicted co-expression of *SYT11* and *LAMA5* – a CMS protein that resides in the basal membrane and is

thought to interact with other synaptic proteins such as SV2, where it binds to highly conserved *N*-glycosylation sites [89]. This co-expression with CMS genes and high expression in neuronal tissues shows that there may be a role for *SYT11* at the NMJ as part of vesicle recycling [90–92]. The combination of the rare genetic variants in two unrelated families, involvement in pathways related to signal transmission, and predicted co-expression with two CMS genes lends strong support to *SYT11* playing a role at the NMJ.

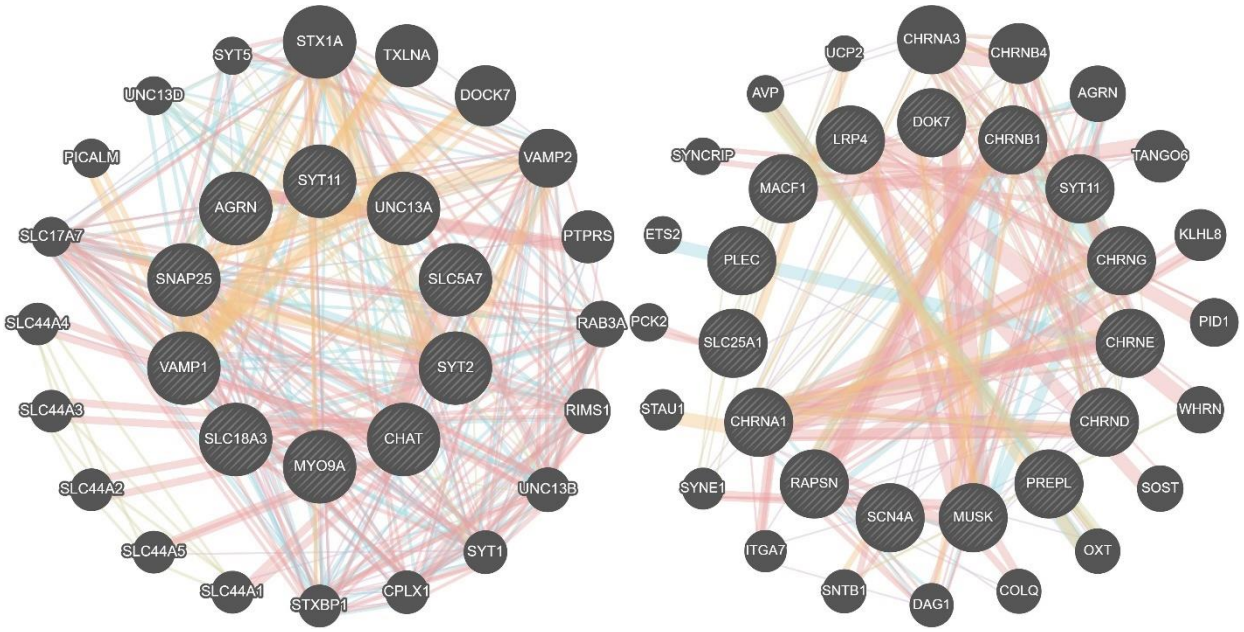

Figure 3.10 - Protein interaction networks of pre- and postsynaptic CMS genes with *SYT11*. These interaction networks show interactions between presynaptic (left) and postsynaptic (right) CMS genes with *SYT11*. The thickness of the lines between nodes (genes) represents the strength of their relationship and the colour represents the type of relationship; common pathways (blue), co-expression (purple), co-localization (violet) protein homology (yellow), physical (pink), genetic (green), and predicted interactions (orange).

3.2.4 Morpholino Co-knockdown of *SYT11* Zebrafish Orthologues *syt11a* and *syt11b*

Having identified strong variants in *SYT11* we proceeded to perform morpholino knockdown studies of zebrafish embryos. Firstly, *SYT11* has two zebrafish orthologues *syt11a* and *syt11b*. We found that both are expressed throughout the first 7 days of development (dpf) and therefore may play a significant role in development and function of the zebrafish neuromuscular

system (Figure 3.11). We began investigation of *SYT11* by determining whether we were able to obtain a successful knockdown of *syt11a* and *syt11b* by using MOs. We designed primer sets to detect intron retention caused by each MO binding to the exon 2/intron 2 border of both genes[80]. For *syt11a* intron detection we used a forward primer spanning the exon 1/2 border and 2 reverse primers; one targeted downstream of the morpholino binding site in intron 2 and a second located at the downstream exon3/4 border (Figure 2.02). For *syt11b* we used two separate primer sets. The first set had an intron 2-specific forward primer and an exon 3-specific reverse primer for detection of *syt11b* knockdown transcript (Figure 2.02). The second set had an exon 2/3-specific forward primer and an exon 3/4-specific reverse primer for detection of native *syt11b* transcripts. We then performed two dose response experiments where we co-injected 2-10ng of *syt11a* or *syt11b* SB MO into WT zebrafish embryos and extracted their RNA at 72 hpf as described in section 2.3.5. From the gels depicted in Figure 3.20 it is evident that detection of intron 2 retention – and therefore our MO knockdown - in *syt11a* (Figure 3.11D) may prove difficult as detection of intron 2 retention was found in WT cDNA. This may occur if there is an unknown splice variant including intron 2, which seems unlikely as no alternative transcripts have been identified in public databases like ensemble, or because of potential contamination of knockdown samples[93]. Intron 2 detection worked well in *syt11b* as there is no band in the untreated WT cDNA and clear intron 2 detection at all doses of *syt11b* MO (Figure 3.11E). Based on these results we determined that a 2-4ng dose of both *syt11a* and *syt11b* SB MO was sufficient for knockdown in zebrafish.

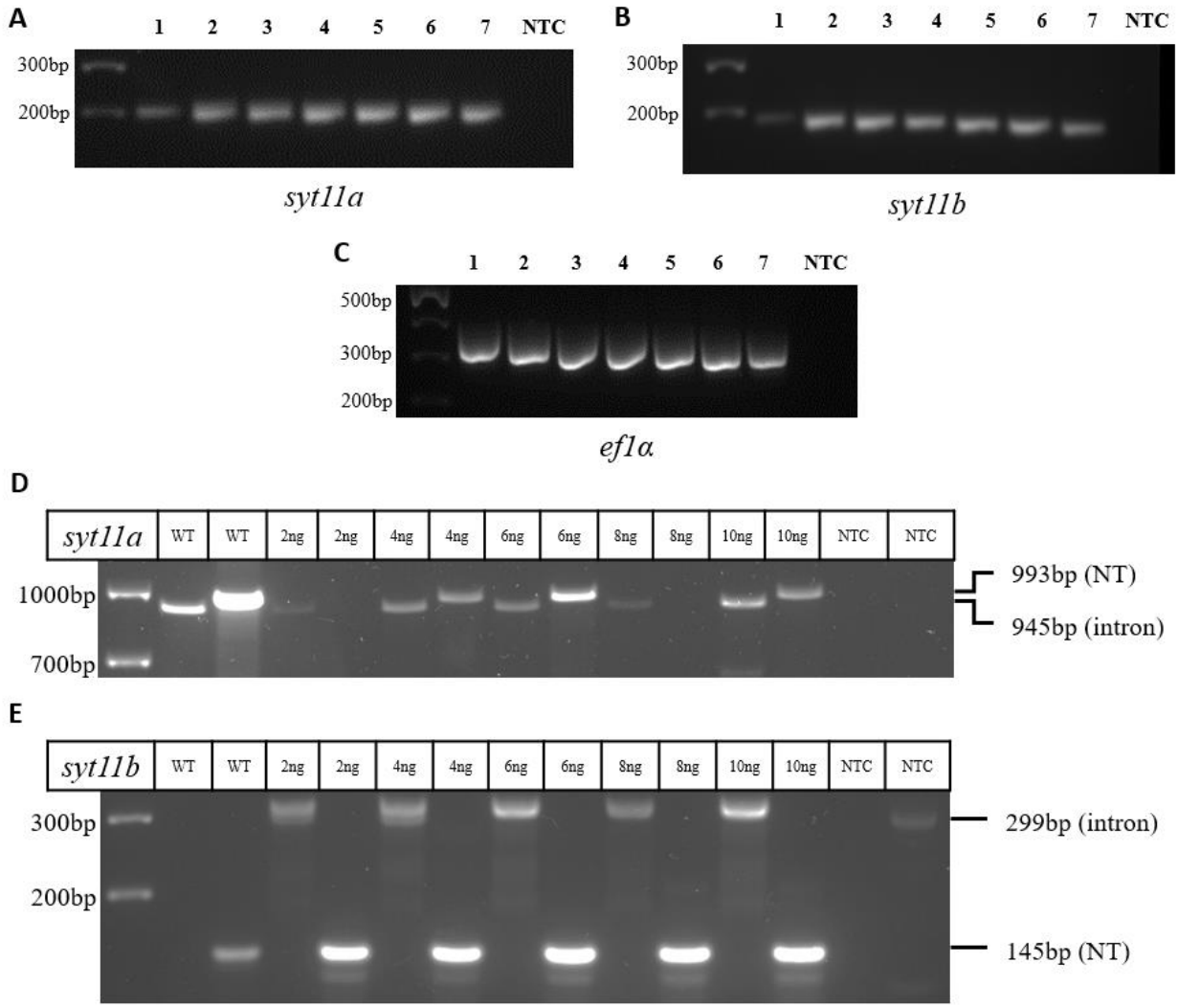

Figure 3.11 – 1-7 dpf expression and morpholino knockdown of of *syt11a* and *syt11b*. The expression of both *syt11a* (A) and *syt11b* (B) from 1-7 days post fertilization (dpf) was done using RT-PCR and both were found to be expressed through the first 7 days of development (NTC = no template control, bp = base pairs) (C) *ef1α* positive control for RT-PCR experiments in A & B. RT-PCR looking for expression of transcripts retaining intron 2 in *syt11a* (D, 945bp) and *syt11b* (E, 299bp) and correctly spliced transcripts (D, 993bp and E, 145bp). WT = wild type cDNA, NT = native transcript.

We began knockdown experiments by co-injecting 4ng of *syt11a* and *syt11b* MOs into WT zebrafish embryos at the 1-4 cell stage of development[65,67,85,86]. At 24hpf these embryos were recorded for 1 minute to observe spontaneous chorion activity. Co-knockdown of these genes using both SB and translation-blocking (TB) MOs showed a significant decrease – and almost complete ablation – of any chorion movement, which points to a strong neuromuscular deficit (Figure 3.12).

Morphological observations at 48 hpf of *syt11a/b* fish showed significant decreases in body length, and eye size (Figure 3.13A-C). Tail curvature was also seen in most knockdown fish (dorsal curve = 3/28, lateral curve = 12/28, ventral curve = 12/28, no curve = 1) whereas only 2 control fish had any tail curvature (lateral curve = 1/27, ventral curve = 1/27, no curve = 25/27). However, tail curvature may be due to non-specific effects of MO knockdown[80,85,94]. We then tested escape response in *syt11a/b* zebrafish as described in section 2.4.2. *syt11a/b* embryos showed a significant reduction in responsiveness to tactile stimulation (Figure 3.14A) and in total distance travelled after stimulus, average velocity, and initial acceleration (Figure 3.14B-D). There are two behaviors which make up our evoked escape response assay: 1) the C-bend, which is the initial bending of the zebrafish body away from the direction of applied stimulus and 2) forward swimming behavior, which is defined by deflection angle of tail oscillations away from the midline of the fish occurring after the initial C-bend [95,96]. Interestingly, the *syt11a/b* zebrafish with severely bent tails that responded to stimulation had an observed reduction in C-bend and tail oscillation size. However, video capture of this behaviour was not suitable for quantitative analysis of these observations because sufficient camera magnification and focus couldn't be achieved to capture this behavior and have a large enough field of view to see the entire escape response. In addition, tail oscillations in some (13/24) *syt11a/b* fish were not strong enough to produce significant movement from their starting point. This weakness caused the embryos to rotate around one spot or in small circles after stimulus (this behavior is represented by the embryo tracking paths from TrackMate in Figure 3.15). However, these behaviors could be non-specific as bent tails are not necessarily caused by co-knockdown of *syt11a/*b[80,85,94]. It is also difficult to conclude if this response is solely caused by NMJ deficits or caused by curved tails as no such responses were seen in fish with straight tails.

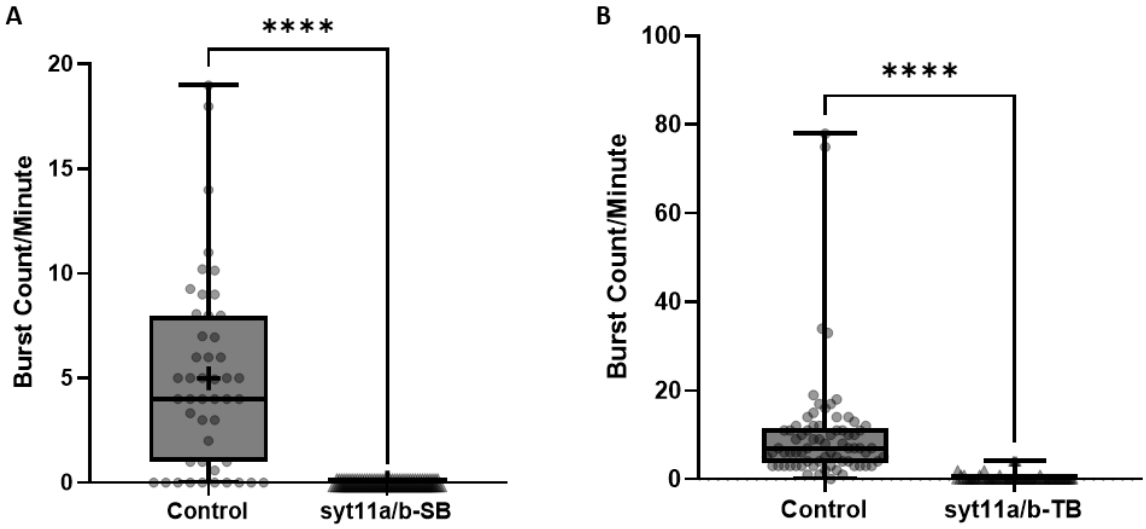

Figure 3.12 - Ablation of chorion activity rate at 24 hpf in *syt11a/b*-splice-blocking (SB) and *syt11a/*b-translation-blocking (TB) morphants. Severe reduction of rotational movement in the chorion was observed at 24 hpf in both (A) SB (Control = 3.99 bursts/min (0.1, 7.99; *n* = 47); *syt11a/b*-SB = 0 bursts/min (0, 0; *n* = 41); Mann Whitney test, ****$P<0.0001$) and (B) TB trials (Control = 6.99 bursts/min (3.5, 11.5; *n* = 73); *syt11a/b*-TB = 0 bursts/min (0, 3.1; *n* = 79); Mann Whitney test, ****$P<0.0001$).

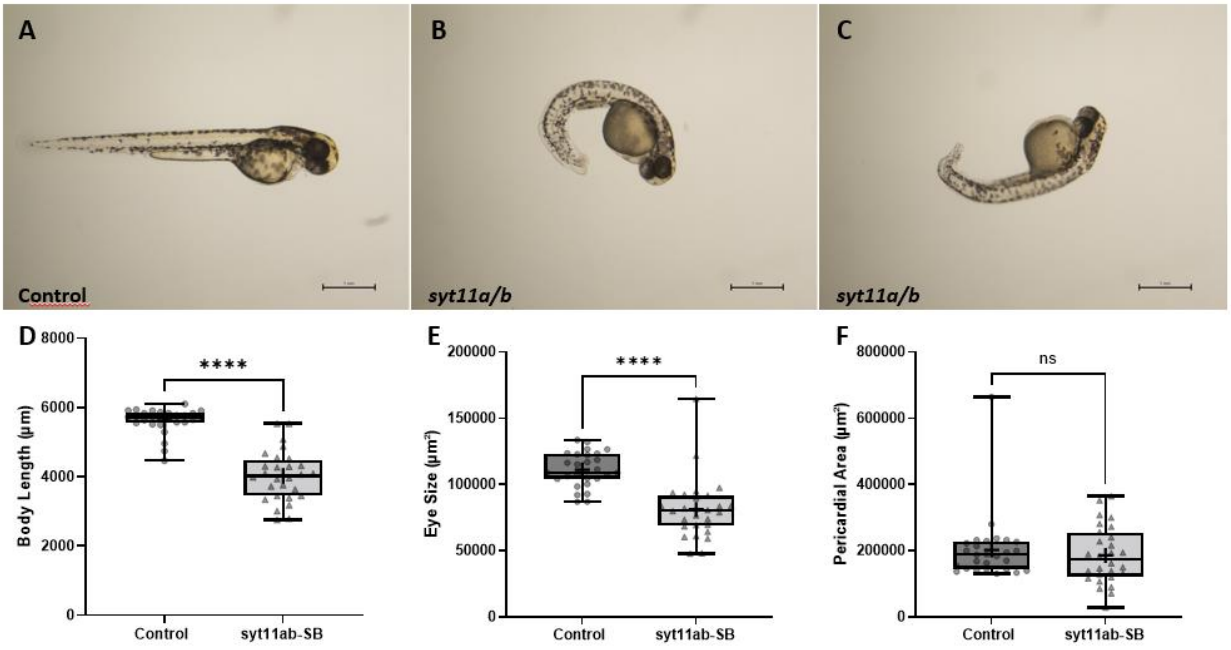

Figure 3.13 –Morphological changes of *syt11a/b*-KD in 48 hpf WT zebrafish. (A) Control injected embryos showed no physical abnormalities. *syt11a/*b KD embryos showed severe tail bends (B & C) and reduced (D) body length (Control = 5718 µm (5554, 5832), *syt11a/b*-SB = 4027 µm (3449,4473); unpaired t-test, ****$P<0.0001$) and (E) eye size (Control = 108820 µm^2 (104417, 122850), *syt11a/b*-SB = 80324 µm^2 (68715, 91347); unpaired t-test, ****$P<0.0001$). (F) No significant difference (ns) was observed in pericardial area in *syt11a/b* KD embryos (Control = 188001 µm^2 (144812, 664468), *syt11a/b*-SB = 172955 µm^2 (122434, 252531); Mann-Whitney test). Control *n* = 27, *syt11a/b n* = 28. Scale Bar = 1 mm.

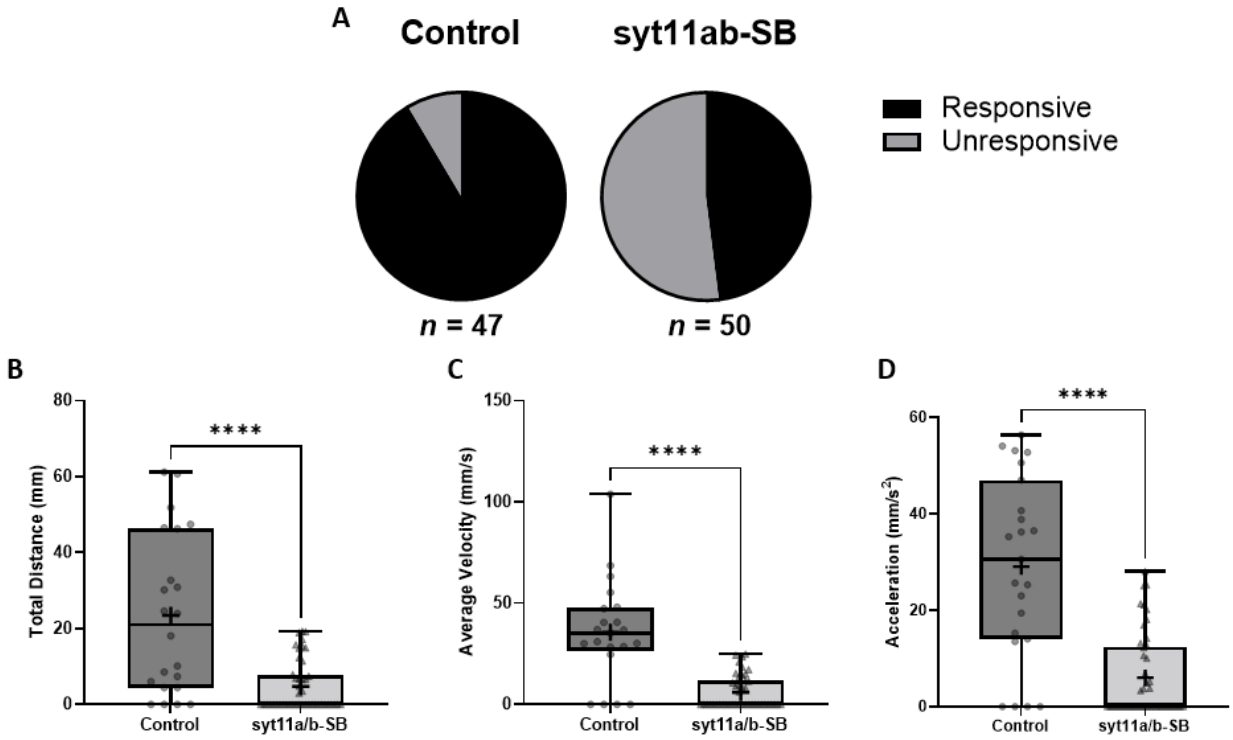

Figure 3.14 – Responsiveness and escape response in 48hpf *syt11a/b* splice-blocking (SB) morphants show loss of locomotion. (A) The responsiveness of *syt11a/b*-SB morphants was significantly reduced (26/50 responsive) compared to controls (43/47 responsive). Significant reductions in (B) total distance traveled (Control = 21 mm (4.42, 46.31), *syt11a/b*-SB = mm; Mann Whitney test, ****$P<0.0001$), (C) average velocity (Control = 35.20 mm/s (26.55, 47.65), *syt11a/b*-SB = 11.76 mm/s (0, 24.93); Mann Whitney test, ****$P<0.0001$) and (D) initial acceleration (Control = 30.60 mm/s^2 (14.04, 56.38), *syt11a/b*-SB = 0 mm /s^2 (0, 12.36); Mann Whitney test, ****$P<0.0001$) were displayed by *syt11a/b* morphants.

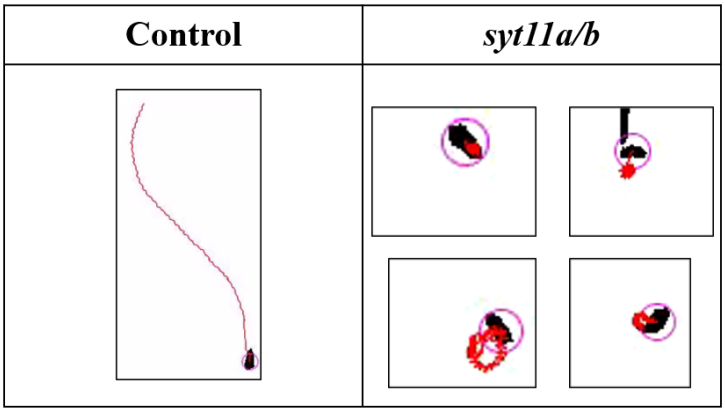

Figure 3.15 – Abnormal rotational behaviour in *syt11a/b* zebrafish. These images are still frames taken from TrackMate during analysis of *syt11a/b* knockdown fish. The control track represents a normal path (red line) control fish typically take. The *syt11a/b* images are taken from 4 different recordings of fish with abnormal rotational responses. These images are representative and not to scale.

The substantial reduction in locomotor ability shown in *syt11a/b* morphants prompted us to perform immunological studies to examine the development of their neuromuscular morphology. Fluorescent staining of AChRs and motor neuron axons revealed a significant reduction in colocalization of pre and postsynaptic components *syt11a/b* fish (Figure 3.16C), suggesting the processes regulating development of NMJs has been disrupted[13,97–99]. This, coupled with data showing a reduced myotome size, myoseptal AChR insertion and proportion of myoseptal innervation, suggest that AChR clustering has been altered (Figure 3.17). There is also a slight yet significant reduction in AChR cluster area (Figure 3.17B) which could point to disruption of the Agrin-MuSK-LRP4 signalling pathway which dictates AChR clustering[97,98,100–102]. Fluorescent staining also revealed that primary motor neuron axons have an abnormal migration pattern as compared to WT embryos (Figure 3.16A&B). Motor anons in the *syt11a/b* morphants are much shorter, less ordered, or even truncated (Fig. 3.16A&B). Reduced innervation, as seen in these fluorescent stains, could explain the decrease in speed and acceleration observed in escape response assays (Figure 3.14).

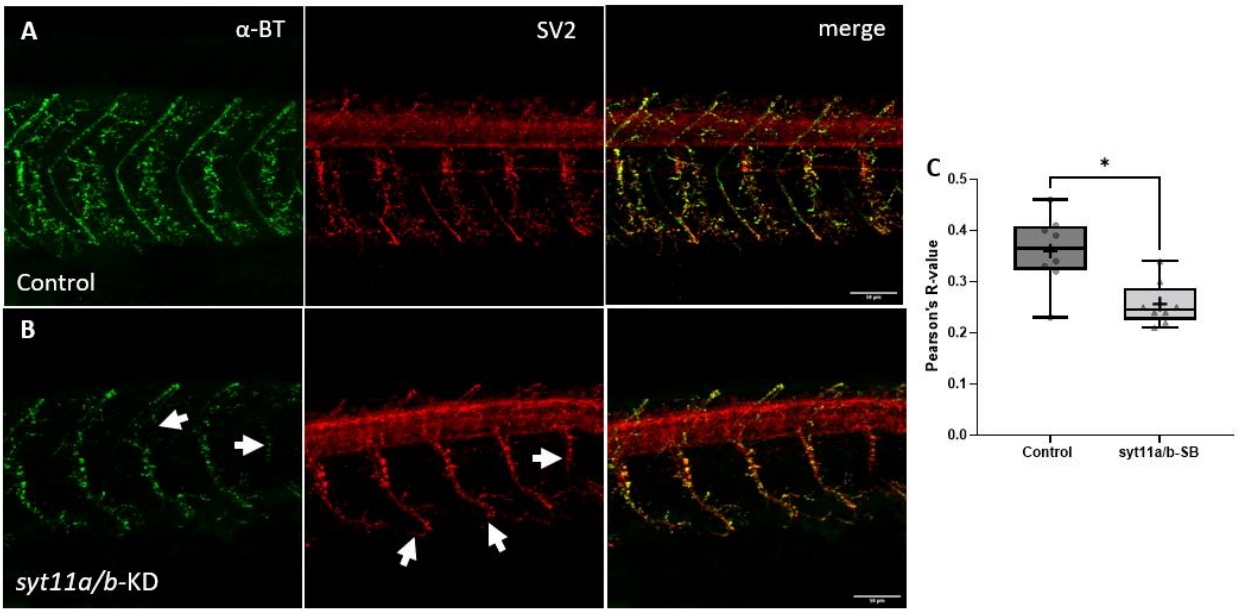

Figure 3.16 – Neuromuscular innervation in *syt11a/b*-KD 48hpf casper zebrafish embryos. (A) Control embryos with fluorescently conjugated α-BT (green) and SV2 (red) show normal myoseptal innervation. Conversely, neuromuscular development in the absence of (B) *syt11a/b* shows shortening of motor axons (arrows in SV2 panel), lack of myoseptal innervation and an overall decrease in AChR staining (arrows in α-BT panel). (C) Morphants also displayed significant reduction of colocalization between AChRs and SV2 (Control = 0.365 (0.323, 0.408; *n* = 8); *syt11a/b*-SB = 0.245 (0.225, 0.288; *n* = 8); Mann Whitney test, **P<0.05*). Scale bar = 50 μm.

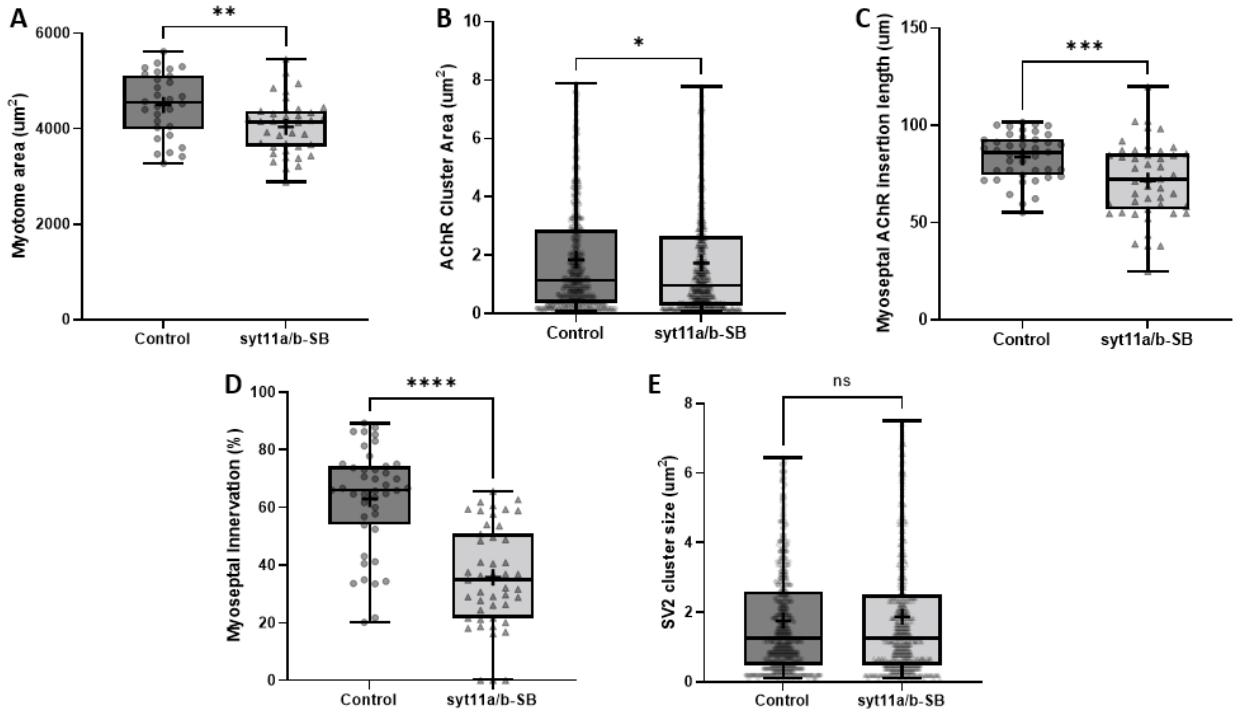

Figure 3.17 - *syt11a/b* knockdown (KD) in 48hpf zebrafish embryos show decreased neuromuscular innervation. Measurements of morphants from Fig. 9 show a significant reduction in (A) myotome area (Control = 4496 (665.6) μm^2, *syt11a/b*-SB = 4036 (573.6) μm^2 (written as mean (SD)), unpaired t-test, ***P<0.01*), (B) myoseptal AChR cluster area (Control = 1.15 μm^2 (0.380, 2.880), *syt11a/b*-SB = 0.960

μm^2 (0.290, 2.665); Mann Whitney test, *$P<0.05$), (C) myoseptal AChR insertion length (Control = 83.83 (12) μm , *syt11a/b*-SB = 71.62 (19.66) μm (written as mean (SD)) ; unpaired t-test, ***$P<0.001$) and (D) myoseptal innervation (Control = 66.03 μm (53.98, 74.32), *syt11a/b*-SB = 34.89 μm (21.70, 50.83); Mann Whitney test, ****$P<0.0001$). (E) No significant difference in SV2 cluster size was observed in *syt11a/b* morphants (Control = 1.25 μm^2 (0.480, 2.59), *syt11a/b-SB* = 1.25 μm^2 (0.480, 2.50); Mann Whitney test). Control n = 8, *syt11a/b*-SB n = 8.

3.2.5 Knockdown of *syt11b* is Sufficient to Cause Neuromuscular Deficit in Zebrafish

Co-knockdown produced a clear neuromuscular phenotype in zebrafish embryos. Further investigation required us to determine if individual knockdown was sufficient to produce the phenotype observed on *syt11a/b* knockdown. So, we performed the same functional studies with single injections of SB or TB morpholino for syt11a and syt11b individually.

Beginning with *syt11a* we measured chorion activity rate at 24 hpf. This revealed that the rate of chorion activity was not significantly different from controls – this finding was replicated with TB MO knockdowns (Figure 3.18A). Then escape response analysis in *syt11a* embryos revealed no significant reduction in responsiveness across both SB and TB trials (Figure 3.18B). There were significant increases in average velocity and acceleration during SB MO trials for *syt11a*, but this difference may be a factor of low sample size, as no significant differences were seen in the TB trials for velocity and acceleration where a much higher sample size was obtained (Figure 3.18C-E). Interestingly, there is a large decrease in total distance travelled in the TB *syt11a* trials (Figure 3.18). The gross morphology of these morphants was not affected by *syt11a* knockdown and no bent tails were observed. Although there was a decrease in total distance travelled, it is not enough to support *syt11a* alone is causing the neuromuscular deficits seen in co-knockdown studies.

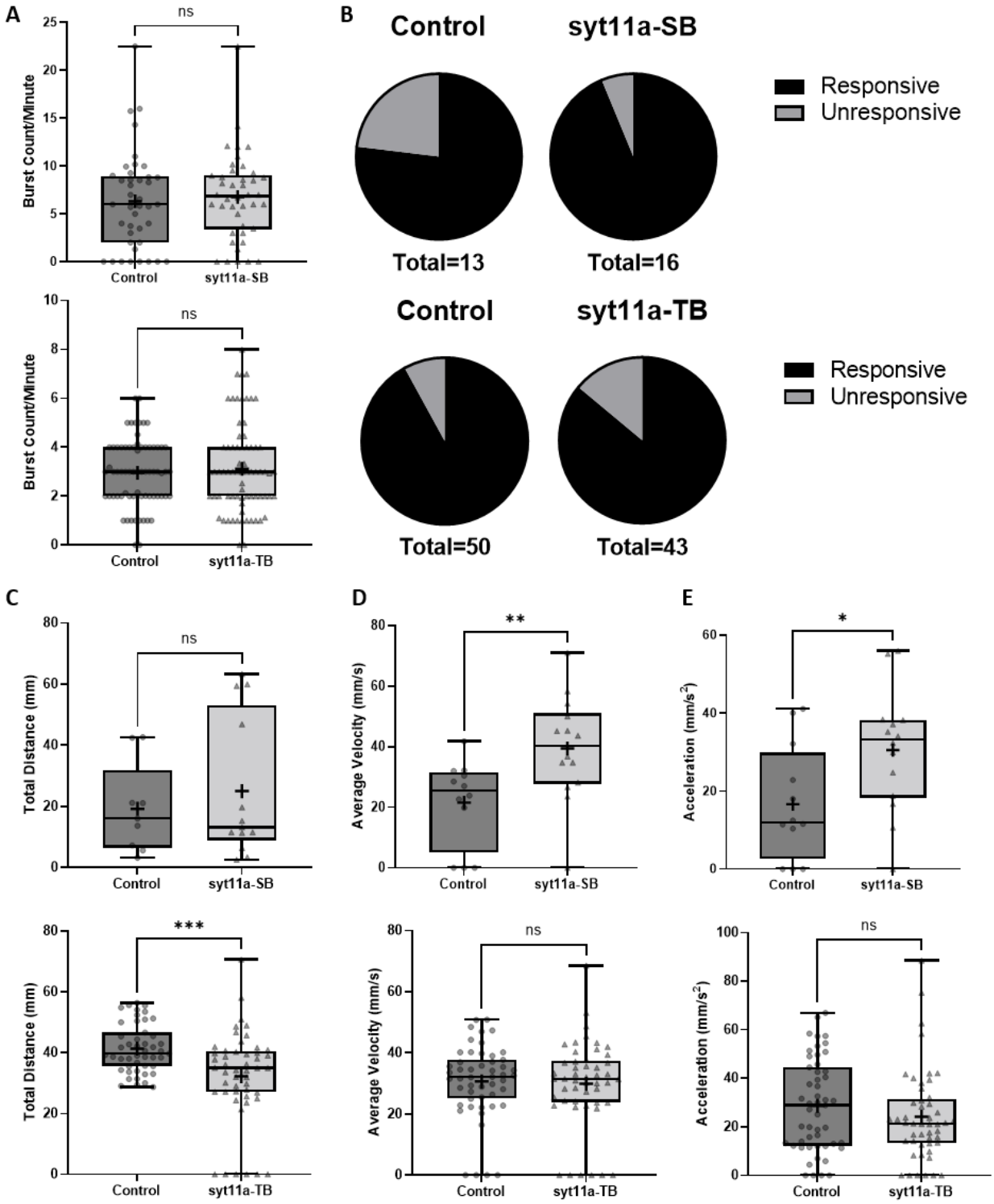

Figure 3.18 - – Chorion activity and escape response in *syt11a*-KD zebrafish embryos with splice-blocking (SB) and translation-blocking (TB) morpholinos (MOs). (A) Activity rate in the chorion at 24 hpf fish were not seen to be significantly different on *syt11a*-KD in either SB (Control = 5.994 bursts/min (1.999, 8.931; *n* = 41); *syt11a*-SB = 6.848 bursts/min (3.346, 9.057; *n* = 42); Mann Whitney test) or TB trials (Control = 2.997 bursts/min (1.998, 3.996; *n* = 69); *syt11a*-TB = 2.997 bursts/min (1.998, 3.996; *n* = 73); Mann Whitney test). (B) *syt11a*-KD also had no effect on responsiveness to tactile stimulus in either

SB trials (Control = 10/13 responsive, *syt11a*-SB = 15/16 responsive) or TB trials (Control = 46/50 responsive, *syt11a*-TB = 37/43 responsive). When *syt11a* knockdown escape response was measured (C) no difference in total distance travelled in SB trials was seen (Control = 16.02 mm (6.442, 31.80), *syt11a*-SB = 13.20 mm (8.909, 53.13); Mann Whitney test) but a significant decrease in TB trials was observed (Control = 39.74 mm (35.59, 46.66), *syt11a*-TB = 34.95 mm (27.03, 40.47); Mann Whitney test, ****P<0.001*). (D) Conversely, a slight significant difference was seen in average velocity of SB trials (Control = 25.43 mm/s (4.969, 31.62), *syt11a*-SB = 40.19 mm/s (27.79, 51.11); Mann Whitney test, ***P<0.01*), but not in TB trials (Control = 32.13 mm/s (24.98, 37.17), *syt11a*-TB = 31.45 mm/s (23.92, 37.41); Mann Whitney test). (E) Initial acceleration measured in SB trials showed slight increase in *syt11a*-SB fish (Control = 12.04 mm/s^2 (2.595, 29.84), *syt11a*-SB = 33.25 mm/s^2 (18.28, 38.29); Mann Whitney test, **P<0.05*) and TB trials showed no change in initial acceleration (Control = 28.92 mm/s^2 (12.24, 44.52), *syt11a*-TB = 21.36 mm/s^2 (13.35, 31.42); Mann Whitney test).

Individual knockdown of *syt11b* was then conducted in the same manner as *syt11a*. The rate of chorion activity was not significantly different to controls at 24hpf when injected with SB MO (Figure 3.19A). However, similarly to co-knockdown trials (Figure 3.14), *syt11b*-TB morphants showed complete absence of chorion activity (Figure 3.19A). This difference between knockdown method could be an indication that the TB MO for *syt11b* is a more effective means of knocking down *syt11b*, although it is difficult to assess its knockdown efficiency - knockdown cannot be measured via RT-PCR and no appropriate zebrafish syt11b antibody has been identified for use in western blot. The morphology of these morphants were like those from co-knockdown trials. Bent tails were seen in 11/25 morphants in *syt11b*-SB trials and 18/25 morphants in *syt11b*-TB trials. Although the severity of bend was less severe in SB morphants than TB morphants. Evidence gathered from *syt11a*-SB trials indicate that this gene is not responsible for inducing movement phenotype we observe in the co-knockdowns, thus it is likely that loss of *syt11b* is having a larger effect on the phenotype. This notion is further supported by the escape response assays which showed significant reductions across all measurements both SB and TB trials (Figure 3.19C-H). Responsiveness in TB trials was also affected as only 3/21 morphants responded to tactile stimulus and agrees with *syt11a/b*-SB and TB studies (Figure 3.19B).

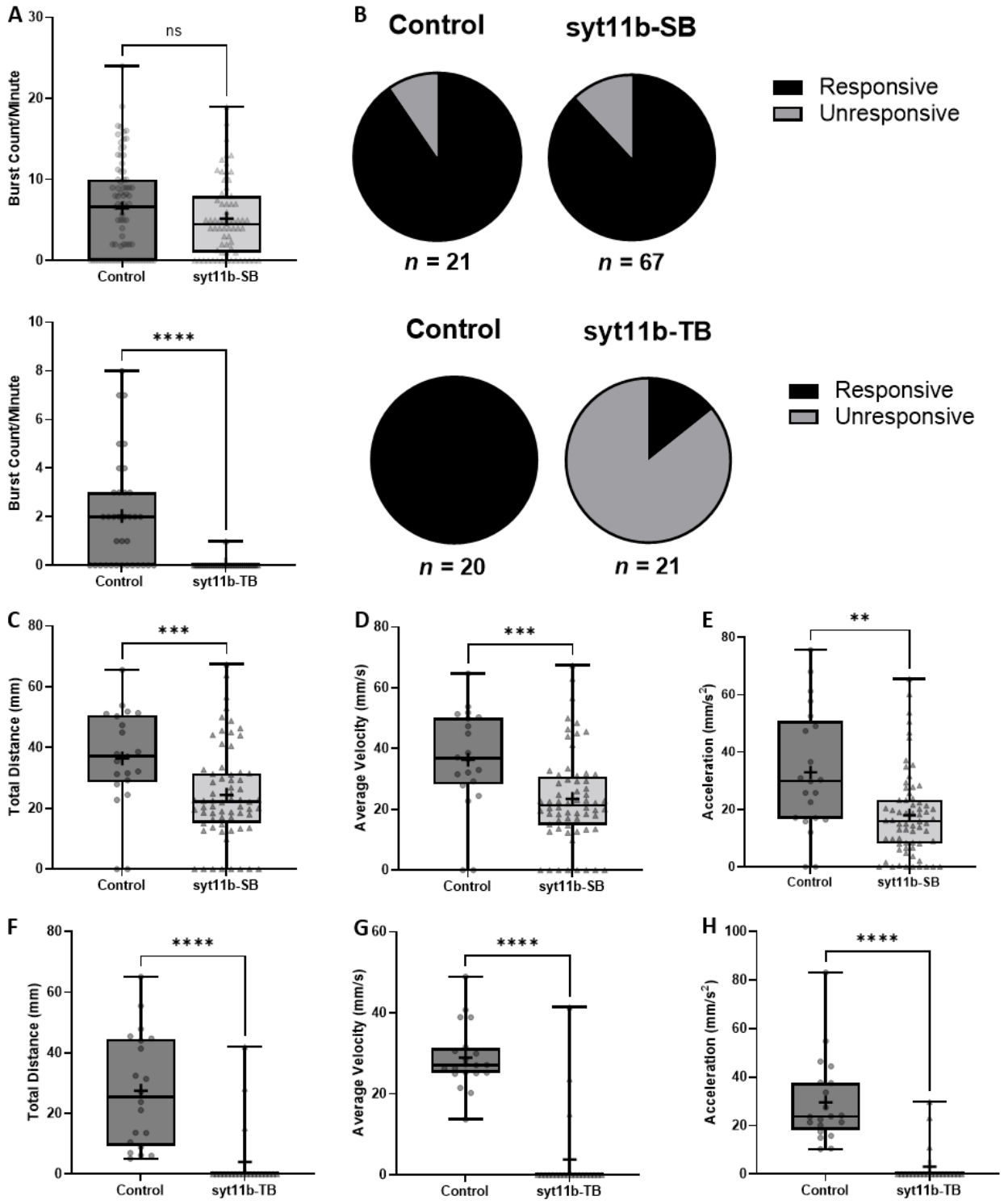

Figure 3.19 - Chorion activity and escape response in *syt11b* zebrafish embryos with splice-blocking (SB) and translation-blocking (TB) morpholinos (MOs). (A) Differential results were found in SB verses TB where in terms of chorion activity as no significant difference is seen in SB MO trials (Control = 6.650 bursts/min (0, 9.990; *n* = 82); *syt11b*-SB = 4.496 bursts/min (0.9990, 7.992; *n* = 74); Mann Whitney test) and embryos in TB trials almost completely stopped moving (Control = 1.998 bursts/min (0, 2.997; *n* = 35); *syt11b*-TB = 0 bursts/min (0, 0; *n* = 31); Mann Whitney test, ****$P<0.0001$). (B) There was almost no

difference in responsiveness to tactile stimulation on *syt11b*-SB knockdown (Control = 19/21 responsive, *syt11b*-SB = 59/67 responsive) whereas embryos treated with *syt11b*-TB MO were much less responsive to touch (Control = 20/20 responsive, *syt11b*-TB = 3/21 responsive). Escape response studies showed *syt11b*-SB had significant reductions in (C) total distance travelled (Control = 37.06 mm (28.59, 50.68), *syt11b*-SB = 22.13 mm (15.06, 31.50); Mann Whitney test, ****P<0.001*), (D) average velocity (Control = 36.80 mm/s (28.27, 50.19), *syt11b*-SB = 21.30 mm/s (14.80, 30.76); Mann Whitney test, ****P<0.001*) and (E) initial acceleration (Control = 29.84 mm/s^2 (16.76, 50.82), *syt11b*-SB = 15.92 mm/s^2 (8.040, 23.28); Mann Whitney test, ***P<0.01*). The *syt11b*-TB trials were almost completely unresponsive to tactile stimulation (Control = 20/20 responsive, *syt11b*-TB = 3/21 responsive) and showed clear differences in (F) total distance traveled (Control = 25.46 mm (9.271, 44.59), *syt11b*-TB = 0 mm (0,0); Mann Whitney test, *****P<0.0001*), (G) average velocity (Control = 27.13 mm/s (25.16, 31.31), *syt11b*-TB = 0 mm/s (0,0); Mann Whitney test, *****P<0.0001*) and (H) initial acceleration (Control = 23.74 mm/s^2 (18.22, 37.71), *syt11b*-TB = 0 mm/s^2 (0,0); Mann Whitney test, *****P<0.0001*).

4. Discussion

This study has taken a translational approach using patient exome sequences to 1) provide a genetic diagnosis for previously unsolved cases by expanding variant filtering criteria, 2) identify rare variants in genes novel to CMS, and 3) link these novel gene candidates to CMS by using a zebrafish model to demonstrate their genetic knockdown causes neuromuscular transmission deficits.

Our cohort analysis involved studying previously analyzed cases to provide new genetic diagnoses and discover new CMS gene candidates. We provided new genetic diagnosis to 12 patients across both cohorts by expanding the variant filtering process to increase population allele frequency and search exome-wide (all genes as compared to curated or HPO-generated gene lists). However, even after relaxing filtering constraints, a substantial number of cases remain unsolved without any variants for further consideration (cohort 1 = 55%, cohort 2 = 49%). Interestingly, the proportion of unsolved cases in this study is similar to other, larger scale, CMS studies[1].

These cases could remain unsolved for a few reasons. WES data, in which only coding regions are sequenced, may not detect so variants lying within deep intronic or other non-coding regions. Copy number variations are also an issue in many rare diseases including CMS[103]. However, copy number variations are difficult to detect with WES and require additional analysis and possibly WGS[58,103]. Pathogenic variants could also be missed if they are in non-disease genes, have no known function, and are not linked with any HPOs. Therefore, a more in-depth study is required to solve these remaining cases. Many will undergo whole genome sequencing to account for possible variants in deep intronic or regulatory regions. Other cases require further clinical investigation to precisely define a patient's phenotype, and – as with patients 35, 65, and 101,

many require parental sequences to confirm variant segregation. However, it is likely that a high proportion of unsolved cases will be solved with yet unknown disease genes.

4.1 *MGAT5B*

The homozygous mutation found in patient 35 caused the amino acid substitution p.Ile290Val. This variant has an AF = 0.0010001 in gnomAD and so just escaped AF thresholds set during primary analysis. This variant is located within the luminal glycosyltransferase domain (family 18) of *MGAT5B* and is predicted to have deleterious effects on protein function. Specifically, this variant is predicted to activate a cryptic splice-donor site which could cause alternative splicing of *MGAT5B*[76]. The high genetic constraint also indicates that *MGAT5B* has a low tolerance for variation and that mutations typically have deleterious effects causing loss of protein function (Table 3-4). A review of the literature revealed that *MGAT5B* itself is a relatively unstudied glycosylation protein. It's primary role is as a regulator of the *O*-mannosyl glycosylation pathway and it has been shown to play a role in integrin-dependent neurite outgrowth of PC12 cells on laminin and collagen substrates – which links this gene to neuronal migration and perhaps growth of motor neurons[104–108]. Defects in the *O*-mannosyl glycosylation pathway have been shown to cause several congenital muscular dystrophies when the glycosylation of dystroglycan is affected. These include congenital muscular dystrophy 1C, limb girdle muscular dystrophy 2I, and Walker Warburg syndrome[109–111]. Muscle Eye Brain Disease (MEB), is caused by mutations in the *POMGnT1* gene – a partner regulator with *MGAT5B* in the *O*-mannosyl pathway[112]. Phenotypically, MEB presents similarly to CMS, but without signal transmission defects. Both MEB and CMS patients may display ocular symptoms, muscle weakness, and intellectual disability[55,113]. With these clinical features in mind, it is interesting that *MGAT5B* has high brain expression but patient 65 does not exhibit any central nervous system (CNS) symptoms[104].

Glycosylation genes like *GFPT1*, *DPAGT1*, *GMPPB*, *ALG2*, and *ALG14* have all been linked to CMS and cause a similar limb-girdle phenotype to the one seen in patient 65[45,114–119]. Additionally, CMS patients with mutations in *GMPPB* and *DPAGT1* often produce a limb-girdle phenotype with or without intellectual disability[46,117]. Therefore, it is possible that defective proteins in the *O*-mannosyl glycosylation pathway lead to this limb-girdle CMS phenotype without intellectual disability in some cases, depending on yet unidentified genetic modifiers or based on mutation type.

Although the *MGAT5B* variant identified suggested *MGAT5B* as a potential CMS gene, our zebrafish studies do not support this as there was no deficit seen in spontaneous chorion movements or escapes response tests. In fact, spontaneous chorion activity rates increased on *mgat5b* knockdown. This may be an indicator of delayed development, but activity returned to control levels after a few hours. An increase in activity rate also means more signals are being transmitted to cause muscle contractions. This is contrary to how fatigable muscle weakness manifests in CMS, by a reduction in signal transmission strength upon sequential stimulation at the NMJ. It is interesting to note that there was increased αBT and SV2 colocalization at 96 hpf on mgtat5b knockdown. This may explain increased chorion activity as increased innervation may have prolonged or increased peak activity rates past the normal peak at 19 hpf to 24 hpf[63]. The increased innervation seen in our immunological studies could be caused by an alternative glycosylation profile of extracellular matrix or signalling proteins, like lamanin β2 and agrin as both are heavily glycosylated proteins and play essential roles in the migration of motor neurons and NMJ development[108,112,120].

With no difference in escape response, a return to control levels of chorion activity, and no quantifiable deficit in neuromuscular development of pre- and postsynaptic structures at 48 hpf,

we can conclude that although interesting, knockdown of *mgat5b* in zebrafish does not produce a significant neuromuscular phenotype that could link its dysfunction with CMS. However, alternative motor axon migration patterns at 48 hpf and increased colocalization at 96 hpf may suggest a phenotype manifests later in development or *mgat5b* is playing a more substantial role in signal transmission or NMJ maintenance rather than NMJ development. It also appears that *mgat5b* function in zebrafish may have a more generalized role than in humans as they only have 1 known coding transcript whereas humans possess 5[93]. Each human transcript that results in a protein could have different signalling sequences designating them for different biological structures such as the NMJ. Therefore, it may be useful to investigate *MGAT5B* dysfunction beyond the effective timeframe of our transient MO knockdown models through use of transgenic technologies such as CRISPR, or by exploring alternative model systems like mice, which are closer in relation to humans[121].

4.2 *SYT11*

In the case of patient 65, the segregation of the homozygous *SYT11* variant causing p.Gly19Ser, is critical to confirming this as a novel CMS gene, as the patient carries a heterozygous p.Arg243Cys variant in *CHRND* (AF = 0.00028). This *CHRND* variant is also reported in ClinVar as a VUS as *in silico* prediction tools like Mutation Taster and SIFT predict it to be damaging, but there is no literature to support this as a pathogenic variant[122,123]. However, both patients' parents are healthy rendering a heterozygous *CHRND* variant with dominant inheritance an unlikely cause, but a *de novo* variant remains a possibility. Parental DNA is required for segregation. There is also an affected nephew in patient 65's family who shows a similar phenotype; however, his DNA has not been sequenced. The second patient with a *SYT11* variant was found in a database-wide search following the initial discovery in patient 65. Patient 101 is unrelated to patient 65, does not have

any family data in GPAP, and their *SYT11* variant is a heterozygous p.His317Tyr located in the C2B domain of *SYT11* and has an AF = 0.000015 with 4 heterozygotes in gnomAD. *SYT2*, another synaptotagmin and known CMS gene, is inherited in both dominant and recessive forms, therefore both heterozygous and heterozygous variants of syt11 were considered for further functional studies[124]. The heterozygous variant may be *de novo*, but parental samples were not available for segregation.

SYT11 codes for the synaptotagmin-11 protein which facilitates vesicle fusion and trafficking at the nerve terminal along with other synaptotagmins, SNARE and SNAP proteins. Several of these synaptotagmins are thought to act as calcium sensors for the quick release of neurotransmitters[87,88,125]. Of the synaptotagmins, *SYT2* is a known CMS gene and plays a role in the calcium-dependent release of ACh at the NMJ[126]. Although not much is known about *SYT11*, there is early evidence showing that it has relationships to neurological diseases such as schizophrenia and Parkinson's, as the gene itself is located within a specific susceptibility locus on chromosome 1[127,128]. In relation to Parkinson's disease, it is thought that the direct ubiquitination of SYT11 or its mTORC1 activation-related decrease in expression, lead to the dysfunction of autophagosome degradation pathways associated with the disease[129]. Structurally, *SYT11* is closely related to *SYT4* and both are considered outliers of the synaptotagmin family due to their reduced ability to bind calcium[130,131]. Patient 65's p.Gly19Ser variant is in a highly conserved transmembrane region (TMR) of SYT11 and experiments show that deletion of this TMR occurs naturally in *SYT1, SYT4, SYT6,* and *SYT7* via exon-skipping and causes trafficking of these proteins to different cellular compartments[132]. Additionally, a *SYT6* mutant (Syt VIΔTM) mimicking an alternatively spliced variant lacking the TMR, caused redirection of SYT6 from the endoplasmic reticulum, Golgi, and plasma membrane towards the cytosol and plasma membrane-

associated structures facing the cytosolic compartment[132]. The natural occurrence of this TMR deletion also suggests that it's removal only affects synaptotagmin localization, not function. Therefore, patient 65's variant may be causing the redirection of SYT11 to a different cellular compartment. *SYT11* is also highly expressed in the brain, which aligns with the neurological phenotypes of schizophrenia and Parkinson's but does not corroborate with our patients phenotypes[131]. A 2016 study by Wang et al, found that *SYT11* is also an inhibitor of clathrin-mediated and bulk endocytosis in mouse dorsal root ganglion neurons – both are pathways critical to achieving efficient vesicle recycling for sustained signal transmission in synapses[90]. Their study also showed that these endocytosis and vesicle recycling pathways increased in activity upon *SYT11* knockdown[90].

Our study focused on knockdown of both *syt11a* and *syt11b* – both individually and together – in zebrafish to establish *SYT11* as a CMS gene. When we knocked down these genes simultaneously using MOs, we found that there was a major reduction in both spontaneous chorion activity and escape response suggesting that these fish suffer from defects in the motor system. We then performed individual knockdown studies of *syt11a* and *syt11b* to determine whether loss of both is required to produce a phenotype or if only one maintains the role of human *SYT11*. Both *syt11a*-SB and TB trials showed no significant deficit in fish locomotor abilities or responsiveness to stimulus. In contrast to this, fish lacking *syt11b* showed a substantial neuromuscular phenotype in all experiments except for chorion activity in *syt11b*-SB trials, where there was a non-significant decrease seen in number of rotations per minute as compared to controls. However, the same fish showed significant deficits during escape response tests. In combination with *syt11b*-TB studies, which showed almost complete ablation of all movements, we believe that these fish showed a

convincing neuromuscular phenotype that could account for the defects observed in co-knockdown studies.

Investigation of neuromuscular development in *syt11a/b* knockdown casper fish showed that their motor axons were significantly shorter or almost completely truncated as compared to controls. Colocalization of SV2 and AChRs was drastically reduced in *syt11a/b* fish, showing much less myotome and myoseptal innervation as their motor neuron axons branched in the opposite direction. These gross morphological features could explain why these fish have locomotor defects, for example if there are not enough NMJs then fish will be unable to stimulate a full muscle contraction. This could be supported by the slight decrease in AChR cluster area seen in *syt11a/b* fish. Smaller AChR cluster size could be an indication of disturbance in the MuSK-LRP4 signalling pathway which dictates AChR clustering at the NMJ[98,101,133]. Although this difference in AChR cluster size is small, it is interesting to note that endosomal trafficking of MuSK is governed by clathrin-dependent endocytosis pathways critical to the differentiation of the pre- and postsynapse of the NMJ[19]. Disruption of this pathway could explain the phenotype seen in our *syt11a/b* fish as genes in the MuSK-LRP4 signalling pathway are important to the NMJ and disruption to them can cause CMS. Public databases like GTEx show human *SYT11* expression to be highest in neuronal tissue and the tibial nerve, making *SYT11* much more likely to cause a presynaptic form of CMS. Conversely, the reduced length of motor neuron axons and reduction in AChR cluster size could be a result of a reduced ability of motor neurons to take up growth factors through endocytosis[90]. This could explain the locomotor issues and would fit within the context of *SYT11* as it is a regulator of both bulk endocytosis and CME[134,135].

Although these studies have provided a substantial amount of evidence supporting *SYT11* as a novel CMS gene, we note that these behavioural tests are not direct measures of signal

transmission and that the effects of these knockdowns may still be non-specific. Up to 20% of MOs have non-specific effects that cause p53 activation and produce morphological and physiological abnormalities[80,85,136]. This p53 activation by MOs may be accounted for by co-injection of a p53-specific MO which has been shown to reduce these non-specific effects[136]. In our single KD studies of *syt11a* and *syt11b* we showed MO KD of *syt11a* had no effect on locomotor ability or morphology. Therefore, *syt11a* is not likely to activate p53 and produce a non-specific phenotype. However, the difference in chorion activity in the *syt11b*-SB and *syt11b*-TB trials showed contradicting results. Co-injection of a p53 and *syt11b* MO may be necessary to show if these differences are non-specific. Additionally, phenotypic specificity may be determined by rescuing the *syt11b* phenotype by co-injection of *syt11b* MO and full length *syt11b* mRNA.

To connect *SYT11* to a CMS phenotype, electrophysiology experiments measuring signal transmission in *syt11b* KD zebrafish could be performed[71,137]. This will allow for demonstration of a decremental response to stimulation at the zebrafish NMJ – a hallmark diagnostic feature of CMS[71,137,138]. Experiments looking to dissect the pathways by which *SYT11* is causing CMS will be paramount, as treatment of CMS patients varies depending on the underlying mechanism of action. These experiments could include the use of patient-derived induced pluripotent stem cells (iPSCs) with either the homozygous p.Gly19Ser or heterozygous p.His317Tyr variant. Patient-derived iPSCs would provide a relevant human cell model which could be differentiated in to motor neurons or muscle cells to examine variant effects on pre and postsynaptic processes like the CME pathway[139–141].

This leads us to consider the mechanism by which *SYT11* could be causing CMS. There are two main possibilities: 1) Increasing the activity of vesicle recycling pathways using CME may cause the release of saturation-levels of ACh into the synapse and cause continuous binding to,

and opening of, postsynaptic AChRs. This would continually depolarize the muscle fibre membrane and make the fibre refractory to sequential stimulus, replicating the decrement of signal seen in CMS patients; which is a similar mechanism to slow-channel myasthenia[142]. This mechanism could be supported by our patients phenotypes as they have symptoms common to slow-channel CMS like scapular winging and ptosis[51]. 2) However, the opposite may be true if synaptic vesicle recycling is being affected. If *SYT11* acts as an inhibitor of clathrin-mediated endocytosis (CME), which is heavily involved in synaptic vesicle recycling, these pathways could lead to an increased rate of synaptic vesicle turnover. Continued turnover could then cause synaptic vesicles to be loaded with less ACh as ACh synthesis and loading mechanisms may not be able to keep pace with vesicle formation[90,128,143,144]. Decreased vesicular ACh also happens in patients with mutations in *CHAT* causing a presynaptic CMS subtype which often presents with episodic apnea – also seen in patient 101[49,50].

4.3 Conclusion

In conclusion, the discovery of two unrelated patients with *SYT11* variants and the evidence presented from these zebrafish studies strongly suggests that *syt11b* causes a neuromuscular phenotype in zebrafish. This phenotype is defined by decreased chorion activity, a compromised escape response likely due to decreased innervation of muscle or signal transmission defects, shortened motor neurons, and reduced AChR cluster size. This phenotype strongly suggests that neuromuscular development is impaired by *syt11b* knockdown and provides a foundation for continued investigation of the potential involvement of *SYT11* in CMS.

5. References

1. Abicht, A. *et al.* Congenital myasthenic syndromes: Achievements and limitations of phenotype-guided gene-after-gene sequencing in diagnostic practice: A study of 680 patients. *Hum. Mutat.* **33**, 1474–1484 (2012).

2. McMacken, G., Abicht, A., Evangelista, T., Spendiff, S. & Lochmüller, H. The Increasing Genetic and Phenotypical Diversity of Congenital Myasthenic Syndromes. *Neuropediatrics* **48**, 294–308 (2017).

3. Catterall, W. A. Voltage-Gated Calcium Channels. *Cold Spring Harb. Perspect. Biol.* **3**, 1–23 (2011).

4. Südhof, T. C. THE SYNAPTIC VESICLE CYCLE. *Annu. Rev. Neurosci.* **27**, 509–547 (2004).

5. Karlin, A. Emerging structure of the Nicotinic Acetylcholine receptors. *Nat. Rev. Neurosci. 2002 32* **3**, 102–114 (2002).

6. Wu, H., Xiong, W. C. & Mei, L. To build a synapse: signaling pathways in neuromuscular junction assembly. *Development* **137**, 1017–1033 (2010).

7. Soreq, H. & Seidman, S. Acetylcholinesterase — new roles for an old actor. *Nat. Rev. Neurosci. 2001 24* **2**, 294–302 (2001).

8. Gasnier, B. The loading of neurotransmitters into synaptic vesicles. *Biochimie* **82**, 327–337 (2000).

9. Bonanomi, D. & Pfaff, S. L. Motor Axon Pathfinding. *Cold Spring Harb. Perspect. Biol.* **2**, (2010).

10. Wu, H., Xiong, W. C. & Mei, L. To build a synapse : signaling pathways in neuromuscular junction assembly. **1033**, 1017–1033 (2010).

11. Kim, M., Bjorke, B. & Mastick, G. S. Motor neuron migration and positioning mechanisms: New roles for guidance cues. *Semin. Cell Dev. Biol.* **85**, 78–83 (2019).

12. Zhang, B. *et al.* Wnt proteins regulate acetylcholine receptor clustering in muscle cells. *Mol. Brain 2012 51* **5**, 1–8 (2012).

13. Panzer, J. A. *et al.* Neuromuscular synaptogenesis in wild-type and mutant zebrafish. *Dev. Biol.* **285**, 340–357 (2005).

14. Panzer, J. A., Song, Y. & Balice-Gordon, R. J. In vivo imaging of preferential motor axon outgrowth to and synaptogenesis at prepatterned acetylcholine receptor clusters in embryonic zebrafish skeletal muscle. *J. Neurosci.* **26**, 934–947 (2006).

15. Gesemann, M., Denzer, A. J. & Ruegg, M. A. Acetylcholine receptor-aggregating activity of agrin isoforms and mapping of the active site. *J. Cell Biol.* **128**, 625–636 (1995).

16. Gautam, M. *et al.* Defective Neuromuscular Synaptogenesis in Agrin-Deficient Mutant Mice. *Cell* **85**, 525–535 (1996).

17. Yang, J.-F., Cao, G., Koirala, S., Reddy, L. V. & Ko, C.-P. Schwann Cells Express Active Agrin and Enhance Aggregation of Acetylcholine Receptors on Muscle Fibers. *J. Neurosci.* **21**, 9572–9584 (2001).

18. Zhu, D. *et al.* Muscle-Specific Receptor Tyrosine Kinase Endocytosis in Acetylcholine Receptor Clustering in Response to Agrin. *J. Neurosci.* **28**, 1688–1696 (2008).

19. Luiskandl, S., Woller, B., Schlauf, M., Schmid, J. A. & Herbst, R. Endosomal trafficking

of the receptor tyrosine kinase MuSK proceeds via clathrin-dependent pathways, Arf6 and actin. *Febs J.* **280**, 3281 (2013).

20. Moransard, M. *et al.* Agrin Regulates Rapsyn Interaction with Surface Acetylcholine Receptors, and This Underlies Cytoskeletal Anchoring and Clustering. *J. Biol. Chem.* **278**, 7350–7359 (2003).

21. Brandon, E. P. *et al.* Aberrant Patterning of Neuromuscular Synapses in Choline Acetyltransferase-Deficient Mice. *J. Neurosci.* **23**, 539–549 (2003).

22. Yumoto, N., Kim, N. & Burden, S. J. Lrp4 is a retrograde signal for presynaptic differentiation at neuromuscular synapses. *Nat. 2012 4897416* **489**, 438–442 (2012).

23. Oentaryo, M. J., Tse, A. C.-K. & Lee, C. W. Neuronal MT1-MMP mediates ECM clearance and Lrp4 cleavage for agrin deposition and signaling in presynaptic development. *J. Cell Sci.* **133**, (2020).

24. DePew, A. T. & Mosca, T. J. Conservation and Innovation: Versatile Roles for LRP4 in Nervous System Development. *J. Dev. Biol. 2021, Vol. 9, Page 9* **9**, 9 (2021).

25. Noakes, P. G., Gautam, M., Mudd, J., Sanes, J. R. & Merlie, J. P. Aberrant differentiation of neuromuscular junctions in mice lacking s-laminin/laminin β2. *Nat. 1995 3746519* **374**, 258–262 (1995).

26. Knight, D., Tolley, L. K., Kim, D. K., Lavidis, N. A. & Noakes, P. G. Functional analysis of neurotransmission at β2-laminin deficient terminals. *J. Physiol.* **546**, 789–800 (2003).

27. González-Ramírez, R. & Felix, R. Transcriptional regulation of voltage-gated Ca2+ channels. *Acta Physiol.* **222**, e12883 (2018).

28. Billings, S. E., Clarke, G. L. & Nishimune, H. ELKS1 and Ca 2+ channel subunit β4 interact and colocalize at cerebellar synapses. *Neuroreport* **23**, 49–54 (2012).

29. Uriu, Y. *et al.* Rab3-interacting Molecule γ Isoforms Lacking the Rab3-binding Domain Induce Long Lasting Currents but Block Neurotransmitter Vesicle Anchoring in Voltage-dependent P/Q-type Ca2+ Channels. *J. Biol. Chem.* **285**, 21750–21767 (2010).

30. Kiyonaka, S. *et al.* RIM1 confers sustained activity and neurotransmitter vesicle anchoring to presynaptic Ca2+ channels. *Nat. Neurosci. 2007 106* **10**, 691–701 (2007).

31. Chen, J., Billings, S. E. & Nishimune, H. Calcium Channels Link the Muscle-Derived Synapse Organizer Laminin β2 to Bassoon and CAST/Erc2 to Organize Presynaptic Active Zones. *J. Neurosci.* **31**, 512–525 (2011).

32. Rieckhof, G. E., Yoshihara, M., Guan, Z. & Littleton, J. T. Presynaptic N-type Calcium Channels Regulate Synaptic Growth *. *J. Biol. Chem.* **278**, 41099–41108 (2003).

33. Feng, Z. & Ko, C.-P. The Role of Glial Cells in the Formation and Maintenance of the Neuromuscular Junction. *Ann. N. Y. Acad. Sci.* **1132**, 19–28 (2008).

34. Darabid, H., Arbour, D. & Robitaille, R. Glial Cells Decipher Synaptic Competition at the Mammalian Neuromuscular Junction. *J. Neurosci.* **33**, 1297–1313 (2013).

35. Faas, M. M., Sáez, T. & de Vos, P. Extracellular ATP and adenosine: The Yin and Yang in immune responses? *Mol. Aspects Med.* **55**, 9–19 (2017).

36. Alvarez-Suarez, P., Gawor, M. & Prószyński, T. J. Perisynaptic schwann cells - The multitasking cells at the developing neuromuscular junctions. *Semin. Cell Dev. Biol.* **104**, 31–38 (2020).

37. H, D., A, S.-P.-S. & R, R. Purinergic-Dependent Glial Regulation of Synaptic Plasticity of Competing Terminals and Synapse Elimination at the Neuromuscular Junction. *Cell Rep.* **25**, 2070-2082.e6 (2018).

38. Todd, K. J., Darabid, H. & Robitaille, R. Perisynaptic Glia Discriminate Patterns of Motor Nerve Activity and Influence Plasticity at the Neuromuscular Junction. *J. Neurosci.* **30**, 11870–11882 (2010).

39. Bruneau, E., Sutter, D., Hume, R. I. & Akaaboune, M. Identification of Nicotinic Acetylcholine Receptor Recycling and Its Role in Maintaining Receptor Density at the Neuromuscular Junction In Vivo. *J. Neurosci.* **25**, 9949–9959 (2005).

40. Rudolf, R. & Straka, T. Nicotinic acetylcholine receptor at vertebrate motor endplates: Endocytosis, recycling, and degradation. *Neurosci. Lett.* (2019). doi:10.1016/j.neulet.2019.134434

41. Babu, K., Hu, Z., Chien, S. C., Garriga, G. & Kaplan, J. M. The Immunoglobulin Super Family Protein RIG-3 Prevents Synaptic Potentiation and Regulates Wnt Signaling. *Neuron* **71**, 103–116 (2011).

42. Son, Y. J. & Thompson, W. J. Schwann cell processes guide regeneration of peripheral axons. *Neuron* **14**, 125–132 (1995).

43. Kang, H., Tian, L., Mikesh, M., Lichtman, J. W. & Thompson, W. J. Terminal Schwann Cells Participate in Neuromuscular Synapse Remodeling during Reinnervation following Nerve Injury. *J. Neurosci.* **34**, 6323–6333 (2014).

44. Petrov, K. A. *et al.* Schwann cells sense and control acetylcholine spillover at the

neuromuscular junction by α7 nicotinic receptors and butyrylcholinesterase. *J. Neurosci.* **34**, 11870–11883 (2014).

45. Belaya, K. *et al.* Mutations in DPAGT1 cause a limb-girdle congenital myasthenic syndrome with tubular aggregates. *Am. J. Hum. Genet.* **91**, 193–201 (2012).

46. Natera-de Benito, D. *et al.* Molecular characterization of congenital myasthenic syndromes in Spain. *Neuromuscul. Disord.* **27**, 1087–1098 (2017).

47. Cruz, P. M. R., Palace, J. & Beeson, D. The Neuromuscular Junction and Wide Heterogeneity of Congenital Myasthenic Syndromes. 1–23 (2018). doi:10.3390/ijms19061677

48. Engel, B. A. G. Congenital Myasthenic Syndromes. 28–30 (2019).

49. Ohno, K. *et al.* Choline acetyltransferase mutations cause myasthenic syndrome associated with episodic apnea in humans. *Proc. Natl. Acad. Sci. U. S. A.* **98**, 2017–2022 (2001).

50. McMacken, G. *et al.* Congenital myasthenic syndrome with episodic apnoea: clinical, neurophysiological and genetic features in the long-term follow-up of 19 patients. *J. Neurol.* **265**, 194–203 (2018).

51. Engel, A. G., Shen, X. M., Selcen, D. & Sine, S. M. Congenital myasthenic syndromes: pathogenesis, diagnosis, and treatment. *Lancet Neurol.* **14**, 420–434 (2015).

52. Kao, J. C. *et al.* Congenital myasthenic syndromes in adult neurology clinic: A long road to diagnosis and therapy. *Neurology* **91**, E1770–E1777 (2018).

53. Garg, N. *et al.* Late presentations of congenital myasthenic syndromes: How many do we

miss? *Muscle Nerve* **54**, 721–727 (2016).

54. Abicht, A. *et al.* A common mutation (ε1267delG) in congenital myasthenic patients of Gypsy ethnic origin. *Neurology* **53**, 1564–1569 (1999).

55. Finsterer, J. Congenital myasthenic syndromes. **5**, 1–22 (2019).

56. O'Connor, E. *et al.* Clinical and research strategies for limb-girdle congenital myasthenic syndromes. *Ann. N. Y. Acad. Sci.* **1412**, 102–112 (2018).

57. J, O. *et al.* MACF1 links Rapsyn to microtubule- and actin-binding proteins to maintain neuromuscular synapses. *J. Cell Biol.* **218**, 1686–1705 (2019).

58. Thompson, R. *et al.* Advances in the diagnosis of inherited neuromuscular diseases and implications for therapy development. *Lancet Neurol.* **19**, 522–532 (2020).

59. Howe, K. *et al.* The zebrafish reference genome sequence and its relationship to the human genome. *Nat. 2013 4967446* **496**, 498–503 (2013).

60. Pappalardo, A. *et al.* Neuromuscular disorders in zebrafish: State of the art and future perspectives. *NeuroMolecular Medicine* **15**, 405–419 (2013).

61. Phillips, J. B. & Westerfield, M. Zebrafish models in translational research: tipping the scales toward advancements in human health. *Dis. Model. Mech.* **7**, 739–743 (2014).

62. Hao, L. T., Wolman, M., Granato, M. & Beattie, C. E. Survival Motor Neuron Affects Plastin 3 Protein Levels Leading to Motor Defects. *J. Neurosci.* **32**, 5074–5084 (2012).

63. Saint-Amant, L. & Drapeau, P. Time course of the development of motor behaviors in the zebrafish embryo. *J. Neurobiol.* **37**, 622–632 (1998).

64. Senderek, J. *et al.* Hexosamine biosynthetic pathway mutations cause neuromuscular transmission defect. *Am. J. Hum. Genet.* **88**, 162–172 (2011).

65. Müller, J. S. *et al.* Dok-7 promotes slow muscle integrity as well as neuromuscular junction formation in a zebrafish model of congenital myasthenic syndromes. *Hum. Mol. Genet.* **19**, 1726–1740 (2010).

66. Carss, K. J. *et al.* Mutations in GDP-mannose pyrophosphorylase B cause congenital and limb-girdle muscular dystrophies associated with hypoglycosylation of α-dystroglycan. *Am. J. Hum. Genet.* **93**, 29–41 (2013).

67. O'Connor, E. *et al.* Identification of mutations in the MYO9A gene in patients with congenital myasthenic syndrome. *Brain* **139**, 2143–2153 (2016).

68. Chaouch, A. *et al.* Mutations in the Mitochondrial Citrate Carrier SLC25A1 are Associated with Impaired Neuromuscular Transmission. *J. Neuromuscul. Dis.* **1**, 75–90 (2014).

69. Walogorsky, M. *et al.* Zebrafish model for congenital myasthenic syndrome reveals mechanisms causal to developmental recovery. *Proc. Natl. Acad. Sci. U. S. A.* **109**, 17711–17716 (2012).

70. Walogorsky, M., Mongeon, R., Wen, H., Mandel, G. & Brehm, P. Acetylcholine Receptor Gating in a Zebrafish Model for Slow-Channel Syndrome. *J. Neurosci.* **32**, 7941–7948 (2012).

71. Wen, H., Hubbard, J. M., Wang, W. C. & Brehm, P. Fatigue in rapsyn-deficient zebrafish reflects defective transmitter release. *J. Neurosci.* **36**, 10870–10882 (2016).

72. Ono, F., Shcherbatko, A., Higashijima, S. ichi, Mandel, G. & Brehm, P. The Zebrafish Motility Mutant twitch once Reveals New Roles for Rapsyn in Synaptic Function. *J. Neurosci.* **22**, 6491 (2002).

73. Lochmüller, H. *et al.* RD-Connect, NeurOmics and EURenOmics: collaborative European initiative for rare diseases. *Eur. J. Hum. Genet. 2018 266* **26**, 778–785 (2018).

74. Thompson, R. *et al.* RD-Connect: An Integrated Platform Connecting Databases, Registries, Biobanks and Clinical Bioinformatics for Rare Disease Research. *J. Gen. Intern. Med. 2014 293* **29**, 780–787 (2014).

75. Robinson, P. & Mundlos, S. The Human Phenotype Ontology. *Clin. Genet.* **77**, 525–534 (2010).

76. Desmet, F.-O. *et al.* Human Splicing Finder : an online bioinformatics tool to predict splicing signals. **37**, 1–14 (2009).

77. Warde-Farley, D. *et al.* The GeneMANIA prediction server: Biological network integration for gene prioritization and predicting gene function. *Nucleic Acids Res.* **38**, 214–220 (2010).

78. Jensen, L. J. *et al.* STRING 8—a global view on proteins and their functional interactions in 630 organisms. *Nucleic Acids Res.* **37**, D412–D416 (2009).

79. Smedley, D. *et al.* Next-generation diagnostics and disease-gene discovery with the Exomiser. *Nat. Protoc. 2015 1012* **10**, 2004–2015 (2015).

80. Eisen, J. S. & Smith, J. C. Controlling morpholino experiments: Don't stop making antisense. *Development* **135**, 1735–1743 (2008).

81. Teng, F. Y. H., Wang, Y. & Tang, B. L. The syntaxins. *Genome Biol.* **2**, reviews3012.1 (2001).

82. O'Connor, E. *et al.* Modulation of Agrin and RhoA Pathways Ameliorates Movement Defects and Synapse Morphology in MYO9A-Depleted Zebrafish. *Cells* **8**, 848 (2019).

83. O'Connor, E. *et al.* MYO9A deficiency in motor neurons is associated with reduced neuromuscular agrin secretion. **27**, 1434–1446 (2018).

84. Arijs, I. *et al.* Mucosal Gene Expression of Antimicrobial Peptides in Inflammatory Bowel Disease Before and After First Infliximab Treatment. *PLoS One* **4**, (2009).

85. Bedell, V. M., Westcot, S. E. & Ekker, S. C. Lessons from morpholino-based screening in zebrafish. *Brief. Funct. Genomics* **10**, 181–188 (2011).

86. Pauli, A., Montague, T. G., Lennox, K. A., Behlke, M. A. & Schier, A. F. Antisense Oligonucleotide-Mediated Transcript Knockdown in Zebrafish. *PLoS One* **10**, e0139504 (2015).

87. Südhof, T. C. Synaptotagmins: Why so many? *Journal of Biological Chemistry* **277**, 7629–7632 (2002).

88. Sü, T. C. & Rizo, J. *Synaptotagmins: C 2-Domain Proteins Review That Regulate Membrane Traffic*. *Neuron* **17**, (1996).

89. Maselli, R. A. *et al.* Presynaptic congenital myasthenic syndrome with a homozygous sequence variant in LAMA5 combines myopia, facial tics, and failure of neuromuscular transmission. *Am. J. Med. Genet. Part A* **173**, 2240–2245 (2017).

90. Wang, C. *et al.* Synaptotagmin-11 inhibits clathrin-mediated and bulk endocytosis. *EMBO*

Rep. **17**, 47–63 (2016).

91. Dittman, J. & Ryan, T. A. Molecular circuitry of endocytosis at nerve terminals. *Annual Review of Cell and Developmental Biology* **25**, 133–160 (2009).

92. Pelassa, I., Zhao, C., Pasche, M., Odermatt, B. & Lagnado, L. Synaptic vesicles are 'primed' for fast clathrin-mediated endocytosis at the ribbon synapse. *Front. Mol. Neurosci.* **7**, (2014).

93. Yates, A. D. *et al.* Ensembl 2020. *Nucleic Acids Res.* **48**, D682–D688 (2020).

94. Nasevicius, A. & Ekker, S. C. Effective targeted gene 'knockdown' in zebrafish. *Nat. Genet.* **26**, 216–220 (2000).

95. Wyart, C. *et al.* Optogenetic dissection of a behavioural module in the vertebrate spinal cord. *Nature* **461**, 407–410 (2009).

96. Liu, K. S. & Fetcho, J. R. Laser ablations reveal functional relationships of segmental hindbrain neurons in zebrafish. *Neuron* **23**, 325–335 (1999).

97. Xing, G. *et al.* A mechanism in agrin signaling revealed by a prevalent Rapsyn mutation in congenital myasthenic syndrome. *Elife* **8**, (2019).

98. Burden, S. J., Huijbers, M. G. & Remedio, L. Fundamental molecules and mechanisms for forming and maintaining neuromuscular synapses. *International Journal of Molecular Sciences* **19**, (2018).

99. Ohkawara, B., Ito, M. & Ohno, K. Molecular Sciences Secreted Signaling Molecules at the Neuromuscular Junction in Physiology and Pathology. *Int. J. Mol. Sci* **22**, 2455 (2021).

100. Bloch-Gallego, E. Mechanisms controlling neuromuscular junction stability. *Cell. Mol. Life Sci.* **72**, 1029–1043 (2015).

101. Barik, A. *et al.* LRP4 is critical for neuromuscular junction maintenance. *J. Neurosci.* **34**, 13892–13905 (2014).

102. Apel, E. D., Glass, D. J., Moscoso, L. M., Yancopoulos, G. D. & Sanes, J. R. Rapsyn is required for MuSK signaling and recruits synaptic components to a musk-containing scaffold. *Neuron* **18**, 623–635 (1997).

103. Wang, W., Wu, Y., Wang, C., Jiao, J. & Klein, C. J. Copy number analysis reveals a novel multiexon deletion of the colq gene in congenital myasthenia. *Neurology: Genetics* **2**, (2016).

104. Inamori, K. ichiro *et al.* Demonstration of the expression and the enzymatic activity of N-acetylglucosaminyltransferase IX in the mouse brain. *Biochim. Biophys. Acta - Gen. Subj.* (2006). doi:10.1016/j.bbagen.2005.11.019

105. Inamori, K. I. *et al.* Molecular Cloning and Characterization of Human GnT-IX, a Novel β1,6-N-Acetylglucosaminyltransferase That Is Specifically Expressed in the Brain. *J. Biol. Chem.* **278**, 43102–43109 (2003).

106. Inamori, K. I. *et al.* N-Acetylglucosaminyltransferase IX Acts on the GlcNAcβ1,2-Manα 1-Ser/Thr Moiety, Forming a 2,6-Branched Structure in Brain O-Mannosyl Glycan. *J. Biol. Chem.* **279**, 2337–2340 (2004).

107. Alvarez-Manilla, G., Troupe, K., Fleming, M., Martinez-Uribe, E. & Pierce, M. Comparison of the substrate specificities and catalytic properties of the sister N-

acetylglucosaminyltransferases, GnT-V and GnT-Vb (IX). *Glycobiology* **20**, 166–174 (2010).

108. Lee, I. *et al.* N-acetylglucosaminyltranferase VB expression enhances beta1 integrin-dependent PC12 neurite outgrowth on laminin and collagen. *J. Neurochem.* **97**, 947–956 (2006).

109. De Bernabé, D. B. V. *et al.* Mutations in the O-mannosyltransferase gene POMT1 give rise to the severe neuronal migration disorder Walker-Warburg syndrome. *Am. J. Hum. Genet.* **71**, 1033–1043 (2002).

110. Yoshida, A. *et al.* Muscular Dystrophy and Neuronal Migration Disorder Caused by Mutations in a Glycosyltransferase, POMGnT1. *Dev. Cell* **1**, 717–724 (2001).

111. Brockington, M. Mutations in the fukutin-related protein gene (FKRP) identify limb girdle muscular dystrophy 2I as a milder allelic variant of congenital muscular dystrophy MDC1C. *Hum. Mol. Genet.* **10**, 2851–2859 (2001).

112. Abbott, K. L., Troupe, K., Lee, I. & Pierce, M. Integrin-dependent neuroblastoma cell adhesion and migration on laminin is regulated by expression levels of two enzymes in the O-mannosyl-linked glycosylation pathway, PomGnT1 and GnT-Vb. *Exp. Cell Res.* **312**, 2837–2850 (2006).

113. Balaraju, S. *et al.* Congenital myasthenic syndrome with mild intellectual disability caused by a recurrent SLC25A1 variant. *Eur. J. Hum. Genet.* **28**, 373–377 (2020).

114. Belaya, K. *et al.* Mutations in GMPPB cause congenital myasthenic syndrome and bridge myasthenic disorders with dystroglycanopathies. 2493–2504 (2015).

doi:10.1093/brain/awv185

115. Selcen, D. *et al.* GFPT1-myasthenia: Clinical, structural, and electrophysiologic heterogeneity. *Neurology* **81**, 370–378 (2013).

116. Cossins, J. *et al.* Congenital myasthenic syndromes due to mutations in ALG2 and ALG14. *Brain* **136**, 944–956 (2013).

117. Öncel, İ. *et al.* DPAGT1 mutation: limb-girdle congenital myasthenic syndrome due to glycosylation defect. *Neuromuscul. Disord.* **24**, 843 (2014).

118. Ohno, K. Glycosylation defects as an emerging novel cause leading to a limb-girdle type of congenital myasthenic syndromes. *Journal of Neurology, Neurosurgery and Psychiatry* **84**, 1064 (2013).

119. Basiri, K. *et al.* Clinical features in a large Iranian family with a limb-girdle congenital myasthenic syndrome due to a mutation in DPAGT1. *Neuromuscul. Disord.* **23**, 469–472 (2013).

120. Dani, N. & Broadie, K. Glycosylated synaptomatrix regulation of trans-synaptic signaling. *Dev. Neurobiol.* **72**, 2–21 (2012).

121. Rubbini, D., Cornet, C., Terriente, J. & Di Donato, V. CRISPR Meets Zebrafish: Accelerating the Discovery of New Therapeutic Targets. *SLAS Discovery* **25**, 552–567 (2020).

122. Schwarz, J. M., Rödelsperger, C., Schuelke, M. & Seelow, D. MutationTaster evaluates disease-causing potential of sequence alterations. *Nat. Methods 2010 78* **7**, 575–576 (2010).

123. Ng, P. C. & Henikoff, S. SIFT: predicting amino acid changes that affect protein function. *Nucleic Acids Res.* **31**, 3812 (2003).

124. Maselli, R. A. *et al.* Dominant and recessive congenital myasthenic syndromes caused by SYT2 mutations. *Muscle Nerve* **64**, 219–224 (2021).

125. DiAntonio, A., Parfitt, K. D. & Schwarz, T. L. Synaptic transmission persists in synaptotagmin mutants of Drosophila. *Cell* **73**, 1281–1290 (1993).

126. Wen, H. *et al.* Distinct roles for two synaptotagmin isoforms in synchronous and asynchronous transmitter release at zebrafish neuromuscular junction. *Proc. Natl. Acad. Sci. U. S. A.* **107**, 13906–13911 (2010).

127. Brzustowicz, L. M., Hodgkinson, K. A., Chow, E. W. C., Honer, W. G. & Bassett, A. S. Location of a major susceptibility locus for familial schizophrenia on chromosome 1q21-q22. *Science (80-.).* **288**, 678–682 (2000).

128. Inoue, S. *et al.* Synaptotagmin XI as a candidate gene for susceptibility to schizophrenia. *Am. J. Med. Genet. Part B Neuropsychiatr. Genet.* **144B**, 332–340 (2007).

129. Bento, C. F., Ashkenazi, A., Jimenez-Sanchez, M. & Rubinsztein, D. C. The Parkinson's disease-associated genes ATP13A2 and SYT11 regulate autophagy via a common pathway. *Nat. Commun.* **7**, (2016).

130. Von Poser, C., Ichtchenko, K., Shao, X., Rizo, J. & Südhof, T. C. The evolutionary pressure to inactivate: A subclass of synaptotagmins with an amino acid substitution that abolishes Ca2+ binding. *J. Biol. Chem.* **272**, 14314–14319 (1997).

131. Dai, H. *et al.* Structural basis for the evolutionary inactivation of Ca2+ binding to

synaptotagmin 4. *Nat. Struct. Mol. Biol.* **11**, 844–849 (2004).

132. Fukuda, M. & Mikoshiba, K. A novel alternatively spliced variant of synaptotagmin VI lacking a transmembrane domain: Implications for distinct functions of the two isoforms. *J. Biol. Chem.* **274**, 31428–31434 (1999).

133. Xing, G., Xiong, W. C. & Mei, L. Rapsyn as a signaling and scaffolding molecule in neuromuscular junction formation and maintenance. *Neuroscience Letters* **731**, (2020).

134. Wang, Y. *et al.* Parkin-dependent and -independent degradation of synaptotagmin-11 in neurons and astrocytes. *Neurosci. Lett.* **739**, 135402 (2020).

135. Shimojo, M. *et al.* Synaptotagmin-11 mediates a vesicle trafficking pathway that is essential for development and synaptic plasticity. *Genes Dev.* **33**, 365–376 (2019).

136. Robu, M. E. *et al.* p53 activation by knockdown technologies. *PLoS Genet.* **3**, 787–801 (2007).

137. Wen, H. & Brehm, P. Paired motor neuron-muscle recordings in zebrafish test the receptor blockade model for shaping synaptic current. *J. Neurosci.* **25**, 8104–8111 (2005).

138. Brehm, P. & Wen, H. Zebrafish neuromuscular junction: The power of N. *Neuroscience Letters* **713**, 134503 (2019).

139. Ababneh, N. A. *et al.* Establishment of (JUCTCi007-A) iPSC line from a patient with congenital myasthenic syndrome (CMS) carrying a homozygous mutation p.Arg331Trp (c.991C > T) in the CHRNE gene. *Stem Cell Res.* **47**, 101906 (2020).

140. Barbeau, S. *et al.* Generation of a human induced pluripotent stem cell line (iPSC) from peripheral blood mononuclear cells of a patient with a myasthenic syndrome due to

mutation in COLQ. *Stem Cell Res.* **49**, 102106 (2020).

141. Zhang, H. *et al.* Generation and characterization of an induced pluripotent stem cell line SDQLCHi018-A from a congenital myasthenic syndrome patient carrying compound heterozygote mutations in RAPSN gene. *Stem Cell Res.* **51**, 102160 (2021).

142. Engel, A. G. & Sine, S. M. Current understanding of congenital myasthenic syndromes. *Curr. Opin. Pharmacol.* **5**, 308–321 (2005).

143. Wang, C. *et al.* Synaptotagmin-11 is a critical mediator of parkin-linked neurotoxicity and Parkinson's disease-like pathology. *Nat. Commun.* **9**, (2018).

144. Jung, N. & Haucke, V. Clathrin-Mediated Endocytosis at Synapses. *Traffic* **8**, 1129–1136 (2007).

6. Appendix I

The text below is the source code as described in section 2.4.2.1 used to analyze ".csv" files containing positional, displacement, and velocity data generated from the ImageJ plugin TrackMate:

```
import csv
import glob
import re

FPS = 240

accelerations_rows = []
averages_rows = []

csv_files = [f for f_ in [glob.glob(e) for e in (
    './**/*.csv', './*.csv')] for f in f_]

for filename in csv_files:
    print('Found CSV file: %s' % (filename))

    if 'averages.csv' in filename:
        continue

    if 'accelerations.csv' in filename:
        continue

    acceleration_segment = re.search(r'(C\d+).+\.csv', filename).group(1)
    frame_initial = None
    frame_final = None
    v_initial = None
    v_final = None
    num_frames = 1

    with open(filename) as csvfile:
        reader = csv.DictReader(csvfile)
        memoized_file = list(reader)
        line_number = 1
        for row in memoized_file:
            if row['VELOCITY'] == 'Infinity':
                line_number += 1
                continue

            current_velocity = float(row['VELOCITY'])

            if frame_initial is None:
                frame_initial = row['Label']
                frame_final = None
            if v_initial is None:
                v_initial = current_velocity
                v_final = None

            if line_number == len(memoized_file):
                frame_final = row['Label']
                v_final = current_velocity
                acceleration = ((v_final - v_initial) * FPS) / num_frames
                accelerations_rows.append(
```

```
                    [acceleration_segment, frame_initial, frame_final, acceleration,
num_frames])
                line_number += 1
                break

            next_row = memoized_file[line_number]

            if next_row['VELOCITY'] == 'Infinity':
                line_number += 1
                continue

            next_velocity = float(next_row['VELOCITY'])

            if current_velocity > next_velocity:
                frame_final = row['Label']
                v_final = current_velocity
                acceleration = ((v_final - v_initial) * FPS) / num_frames
                accelerations_rows.append(
                    [acceleration_segment, frame_initial, frame_final, acceleration,
num_frames])
                frame_initial = None
                v_initial = None
                num_frames = 1
            else:
                num_frames += 1

            line_number += 1

        v_running_total = 0
        d_running_total = 0
        n = 0

        n = len(memoized_file)
        for x in memoized_file:
            v_running_total += float(x['VELOCITY'])
            d_running_total += float(x['DISPLACEMENT'])
        averages_rows.append([
            acceleration_segment,
            d_running_total,
            FPS * v_running_total / n,
        ])

with open('accelerations.csv', 'w') as csvfile:
    writer = csv.writer(csvfile)
    writer.writerow(['fish_id', 'initial_time',
                     'final_time', 'acceleration', 'num_frames'])
    for output_row in accelerations_rows:
        writer.writerow(output_row)

with open('averages.csv', 'w') as csvfile:
    writer = csv.writer(csvfile)
    writer.writerow(['fish_id', 'total_displacement', 'avg_velocity'])
    for output_row in averages_rows:
        writer.writerow(output_row)
```